Role of Gravity Waves in a Vortex-Split Sudden Stratospheric Warming in January 2009

BYEONG-GWON SONG

Division of Polar Climate Sciences, Korea Polar Research Institute, Incheon, South Korea

HYE-YEONG CHUN

Department of Atmospheric Sciences, Yonsei University, Seoul, South Korea

IN-SUN SONG

Division of Polar Climate Sciences, Korea Polar Research Institute, Incheon, South Korea

(Manuscript received 11 February 2020, in final form 20 July 2020)

ABSTRACT: The role of gravity waves (GWs) in a sudden stratospheric warming (SSW) event that occurred in January 2009 (SSW09) is investigated using the MERRA-2 dataset. Nearly 2 weeks prior to the central date (lag = 0), at which the zonal-mean zonal wind at 10 hPa and 60°N first becomes negative, westward GW drag (GWD) is significantly enhanced in the lower mesosphere and stratosphere. At 5 days before lag = 0, planetary waves (PWs) of zonal wavenumber 2 (ZWN-2) in the stratosphere are enhanced, while PWs of ZWN-1 are weakened, which are evident from the amplitudes of the PWs and their Eliassen–Palm flux divergence (EPD). To examine the relationship between PWs and GWs, a nonconservative GWD (NCGWD) source term of the linearized quasigeostrophic potential vorticity equation is considered. A ZWN-2 pattern of the NCGWD forcing is developed around $z = 55$–60 km with a secondary peak around $z = 40$ km just before the PWs of ZWN-2 in the stratosphere began to enhance. A significant positive correlation between the NCGWD forcing in the upper stratosphere and lower mesosphere (USLM; 0.3–0.1 hPa in the present data) and the PWs of ZWN-2 in the stratosphere (5–1 hPa) exists. This result demonstrates that the amplification of the PWs of ZWN-2 in the stratosphere before the onset of SSW09 is likely related to the generation of PWs by GWD in the USLM, which is revealed by the enhanced downward-propagating PWs of ZWN-2 into the stratosphere from above.

KEYWORDS: Gravity waves; Planetary waves; Potential vorticity; Stratospheric circulation; Waves, atmospheric; Middle atmosphere

1. Introduction

Sudden stratospheric warmings (SSWs) are dramatic phenomena associated with rapid temperature increases and polar vortex breakdown in the high-latitude winter stratosphere, which cannot only affect large-scale circulations in the stratosphere (Holton 1980) but also in the troposphere (Baldwin and Dunkerton 2001). SSWs have been categorized into two types based on the vortex structure change in the evolution of SSWs: vortex-displacement and vortex-split types (Charlton and Polvani 2007; Butler et al. 2017). These two types of SSWs have distinct characteristics in planetary waves (PWs) and gravity waves (GWs), as well as the mean wind and temperature (Albers and Birner 2014; Song and Chun 2016). More rapid warming and more abrupt breaking of the polar vortex in the stratosphere are observed for vortex-split SSWs (Charlton and Polvani 2007; Harada et al. 2010; Bancalá et al. 2012; Song and Chun 2016; Butler et al. 2017). Among the various vortex-split type SSW events that occurred during the last approximately 30 years (Charlton and Polvani 2007; Song and Chun 2016), the event that occurred on 24 January 2009 (hereafter SSW09) was the strongest, with temperatures higher than 265 K over the polar regions (Manney et al. 2009; Harada et al. 2010). Around the central date of SSW09, at which the zonal-mean zonal wind at 10 hPa and 60°N first becomes negative, the polar vortex is separated into the two located in North America and central Siberia filled with cold air (Harada et al. 2010).

SSW is a dynamical phenomenon accompanying enormous changes in atmospheric waves as well as those in the mean wind and temperature. Since Matsuno (1971), it has been generally accepted that the interaction between the mean flow and vertically propagating PWs generated from the troposphere is the essential dynamical mechanism for SSWs (Andrews et al. 1987). Enhanced wave fluxes from the troposphere into the stratosphere and breaking of PWs with zonal wavenumbers (ZWN) 1 and 2 in the stratosphere have been considered to be responsible for generating the vortex-displacement and the vortex-split SSWs, respectively. However, some recent studies have noted that enhanced PWs alone may not be sufficient to explain the occurrence of SSWs, and the role of GWs has emerged as an additional wave forcing to drive SSW evolution based on various observations (e.g., Whiteway et al. 1997; Duck et al. 1998, 2001; Wang and Alexander 2009), numerical modeling (e.g., Limpasuvan et al. 2011; Gavrilov et al. 2018; Scheffler et al. 2018), and reanalysis data analyses (e.g., Albers and Birner 2014; Song and Chun 2016). Whiteway et al. (1997)

Supplemental information related to this paper is available at the Journals Online website: https://doi.org/10.1175/JAS-D-20-0039.s1.

Corresponding author: Hye-Yeong Chun, chunhy@yonsei.ac.kr

DOI: 10.1175/JAS-D-20-0039.1

revealed that GW activities observed by Rayleigh lidar were enhanced along the vortex edge during the evolution of SSWs, and Wang and Alexander (2009) obtained similar results using *CHAMP*/GPS satellite data. Based on mesoscale simulations, Limpasuvan et al. (2011) showed that significant negative drag due to the breaking of orographic GWs in the upper stratosphere contributes to the deceleration of the polar westerly jet before the onset of the 2009 major warming. Song and Chun (2016) investigated the contribution of GWs to the evolution of 22 SSW events selected from four global reanalysis datasets.

Recently, the contribution of GWs to SSW in association with PWs has been investigated. As GW drag (GWD) changes the mean flow in the transformed Eulerian mean (TEM) equation, along with the planetary wave forcing represented by Eliassen–Palm (EP) flux divergence (EPD), PWs are modulated by GWs either through changes in the wave propagation condition (Cohen et al. 2014) or by triggering the instability and resonance of PWs (Albers and Birner 2014; Scheffler et al. 2018). Cohen et al. (2014) noted that GWs play a major role in PW modulation in the winter stratosphere through changes in the waveguide of PWs. Albers and Birner (2014) showed that GWD can be a key element for vortex splitting SSW events by preconditioning the polar vortex structure toward its Rossby wave resonance excitation condition. Scheffler et al. (2018) also showed that GWs can significantly contribute to preconditioning the polar vortex by triggering a self-tuned resonance of PWs for the Southern Hemisphere (SH) major SSW that occurred on September 2002. Sato and Nomoto (2015) demonstrated the contribution of GWD to the PWs in the Northern Hemisphere (NH) winter mesosphere that are generated in situ by barotropic/baroclinic instability processes, resulting from the secondary circulation induced by anomalously strong negative GW forcing.

Apart from relation to interaction with PWs as in previous studies, GWD itself can generate PWs in the middle atmosphere as a nonconservative source of the potential vorticity (PV) equation (Andrews et al. 1987). Perhaps the first study on the generation of PWs by GWD in the middle atmosphere was by Holton (1984) to explain the NH winter flow. Using a simple general circulation model (GCM), Holton (1984) well demonstrated that mesospheric PWs are generated by zonally asymmetric GWD (orographic GWD in his case) in the mesosphere that propagate through a zonally symmetric stratospheric wind where originally no PWs exist. The amplitude of the PW generated is maximum in the mesosphere where the GWD is maximum, and it extends down to the stratosphere (Fig. 4 of Holton 1984) with a nearly barotropic structure. McLandress and McFarlane (1993) extended the work of Holton (1984) based on the zonal-mean and linearized perturbation PV equations using the orographic GWD parameterization by McFarlane (1987). Using systematic numerical experiments with and without tropospheric PWs propagating into the middle atmosphere as the lower boundary condition, as well as turning on and off the in situ generation of PW from GWD in the middle atmosphere, McLandress and McFarlane (1993) showed that the amplitude of PWs and resultant EPD in the NH winter middle atmosphere are strongly related to the in situ generation of PWs through the zonally asymmetric GWD forcing and its relative location with respect to vertically propagating PWs from the troposphere. Smith (2003) also showed that stationary PWs in the winter mesosphere can be generated from GWD, and the amplitudes of the in situ generated PWs in the upper mesosphere are larger than those of vertically propagating PWs from the troposphere.

In this study, we examine the role of GWs on a vortex-split-type SSW (SSW09), focusing on the nonconservative GWD forcing of the PV equation during the pre-SSW period, using the Modern-Era Retrospective Analysis for Research and Applications, version 2 (MERRA-2; Gelaro et al. 2017). SSW09 is chosen as the best SSW case to examine the interaction between PWs and GWs, given that SSW09 was characterized by strong GW activities along the polar vortex before the SSW occurrence (Thurairajah et al. 2010; Yamashita et al. 2010; Limpasuvan et al. 2011; Albers and Birner 2014; Song and Chun 2016). The outline of the present paper is as follows. In section 2, MERRA-2 data used in the present study and the definition of SSW are described. Formulations of the EP flux and EPD as well as the TEM equation are given. Residual mean circulations induced by PWs and GWs based on the generalized downward control principle (Haynes et al. 1991) are also described. In section 3, the zonal-mean zonal wind and temperature and wave fields (both PWs and GWs) during the evolution of SSW09 are presented. In section 4, characteristics of the nonconservative GWD (NCGWD) forcing of the linearized quasigeostrophic PV (QGPV) equation in the middle atmosphere are presented, and the correlation between the NCGWD forcing in the lower mesosphere and PW of ZWN-2 in the stratosphere is examined. The amplification of ZWN-2 PWs associated with downward-propagating PWs generated by GWD in the USLM is also presented using the Fourier decomposition method. Finally, a summary and discussion is given in section 5.

2. Data and methodology

In this study, MERRA-2 data (Gelaro et al. 2017) from 1980 to 2015 (36 years) with a horizontal resolution of 0.625° × 0.5° (longitude × latitude) and a temporal resolution of 3 h are used. The zonal wind (u), meridional wind (v), vertical wind (w), temperature (T), geopotential height (h), and the zonal and meridional components of the parameterized GWD (hereafter GWD_X and GWD_Y, respectively) from the surface up to 0.1 hPa are used. The GWD provided from MERRA-2 is the sum of the orographic GWD by the McFarlane (1987) parameterization scheme and the nonorographic GWD by the Garcia and Boville (1994) parameterization scheme. The phase speeds of the nonorographic GWs at the source level (400 hPa) in Garcia and Boville (1994) range from -40 to $+40\ \mathrm{m\ s^{-1}}$ with intervals of $10\ \mathrm{m\ s^{-1}}$. In MERRA-2, the orographic GWD parameterization is modified from the original McFarlane (1987) scheme for better simulation of the seasonal transition of the southern polar night jet, and the nonorographic GWD parameterization is tuned for internally generated quasi-biennial oscillations (Molod et al. 2012). All results presented in the current study are based on the daily average. Any anomaly field is defined as the departure from the daily climatology of 36 years (1980–2015). Note that the daily climatology can be obtained

using either the data from all years, as in the present study, or the non-SSW years exclusively, which was as done in Albers and Birner (2014). Therefore, any anomaly field during the evolution of a certain SSW event that is calculated using the climatology defined by all years data should be smaller than that by the non-SSW years exclusively. The data shown in most figures in the present study are from 1 December 2008 to 31 January 2009, focusing on the behavior of PWs and GWs before the onset of SSW09.

a. SSW definition

A central date of the SSW (hereafter lag = 0) is defined following the criteria of Charlton and Polvani (2007). Note that lag = $-N$ (lag = $+N$) hereafter implies days before (after) the central date. The SSW09 event is classified as a vortex-split SSW based on the criteria of Charlton and Polvani (2007), which corresponds to the type-2 SSW based on the criteria of Ryoo and Chun (2005).

b. TEM equation

The changes in the zonal-mean zonal wind during SSW09 are represented by the TEM momentum equation (Andrews et al. 1987):

$$\frac{\partial \overline{u}}{\partial t} - \overline{v}^* f_a + \overline{w}^* \frac{\partial \overline{u}}{\partial z} = \mathrm{EPD} + \overline{\mathrm{GWD}_X} + \overline{X_r}, \tag{1}$$

$$\mathrm{EPD} = \frac{1}{\rho_0 a \cos\phi} \nabla \cdot \mathbf{F} = \frac{1}{\rho_0 a \cos\phi} \times \left\{ \frac{1}{a\cos\phi} \frac{\partial}{\partial \phi} [F^{(\phi)} \cos\phi] + \frac{\partial F^{(z)}}{\partial z} \right\}, \tag{2}$$

$$F^{(\phi)} = \rho_0 a \cos\phi \left(\frac{\partial \overline{u}}{\partial z} \frac{\overline{v'\theta'}}{\partial \overline{\theta}/\partial z} - \overline{u'v'} \right), \tag{3}$$

$$F^{(z)} = \rho_0 a \cos\phi \left(f_a \frac{\overline{v'\theta'}}{\partial \overline{\theta}/\partial z} - \overline{u'w'} \right). \tag{4}$$

Here, the overbar denotes a zonal mean, and the prime denotes a departure from the zonal mean. The variables are defined as follows: f_a is a term including the Coriolis parameter (f), given by $f_a = f - \partial(\overline{u}\cos\phi)/(a\cos\phi)\partial\phi$; ρ_a is the reference density given as a function of the log-pressure height (z), defined as $z = -H\ln(p/p_s)$, a is the radius of Earth; ϕ is latitude; H is atmospheric-scale height ($H = 7$ km); and p and p_s are the air pressure and surface pressure ($p_s = 1000$ hPa), respectively. The last term in (1), $\overline{X_r}$, is a residual term of the TEM momentum equation, which may contain unresolved wave forcing in the model and imbalance from the analysis increment. The EP flux $\mathbf{F}$ is split into $F^{(\phi)}$ and $F^{(z)}$, the meridional and vertical components, respectively; and $\overline{v}^*$ and $\overline{w}^*$ are the residual mean meridional and vertical velocity components, respectively, which are given as follows:

$$\overline{v}^* = \overline{v} - \frac{1}{\rho_0} \frac{\partial}{\partial z} \left(\frac{\rho_0 \overline{v'\theta'}}{\partial \overline{\theta}/\partial z} \right), \tag{5}$$

$$\overline{w}^* = \overline{w} + \frac{1}{a\cos\phi} \frac{\partial}{\partial \phi} \left(\cos\phi \frac{\overline{v'\theta'}}{\partial \overline{\theta}/\partial z} \right). \tag{6}$$

The residual mean meridional and vertical velocity components induced by each wave forcing can be obtained by the generalized downward control principle (Randel et al. 2002; Chun et al. 2011):

$$\overline{v}^* = -\frac{1}{\rho_0 a \cos\phi} \frac{\partial}{\partial z} \times \left[-\cos\phi \int_z^\infty \rho_0 \left(\frac{\mathrm{EPD} + \overline{\mathrm{GWD}_X} + \overline{X_r} - \frac{\partial \overline{u}}{\partial t}}{f_a} \right) dz' \right], \tag{7}$$

$$\overline{w}^* = \frac{1}{\rho_0 a \cos\phi} \frac{\partial}{\partial \phi} \times \left[-\cos\phi \int_z^\infty \rho_0 \left(\frac{\mathrm{EPD} + \overline{\mathrm{GWD}_X} + \overline{X_r} - \frac{\partial \overline{u}}{\partial t}}{f_a} \right) dz' \right]. \tag{8}$$

Vertical integration is carried out from z to the top of the MERRA-2 data (0.1 hPa), although it should theoretically be to the top of the atmosphere. We found that the differences in $\overline{v}^*$ and $\overline{w}^*$ between (5) and (6) and (7) and (8) are negligible in the mid- and high latitudes where SSW is considered most, and thus, $\overline{v}^*$ and $\overline{w}^*$ obtained by (7) and (8) are used here (see Fig. 6).

3. Results

a. Wind and temperature changes during SSW09

Figure 1a shows the evolution of the horizontal wind speed at 10 hPa during 15–27 January 2009, corresponding to lag = −9 to lag = +3. The elliptical structure of the polar vortex surrounding the Arctic appears at lag = −9, and a horizontally extended vortex structure is seen at lag = −3, as the elliptical structure gradually collapses. The central part of the ellipse is squeezed, and the vortex suddenly splits into two parts at lag = 0, which is sustained until lag = +3. Cold air with temperatures lower than 200 K is located near polar regions with elliptical structures at lag = −9 and −6 (Fig. 1b). At lag = −3, the cold air splits into air masses over central Siberia and North America, and the warm air permeates into the polar regions. At lag = 0, the temperature in the polar region is 50 K higher than that at lag = −9. The vortex splitting structure during the evolution of SSW09 shown in Fig. 1 is consistent with that reported by Harada et al. (2010) using the Japanese 25-year Reanalysis Project (JRA-25; Onogi et al. 2007).

Figure 2 shows the zonal-mean zonal wind at 60°N and polar-cap averaged (60°–90°N) temperature above $z = 5$ km from 1 December 2008 to 31 January 2009, along with their anomalies from the 36-yr climatology. The pink vertical solid lines denote the central date (lag = 0), and the black and brown dots in Figs. 2c and 2d represent the regions where the anomalies are statistically significant at 90% and 95% confidence level, respectively. The westerly jets (Figs. 2a,c) are enhanced during 26 December–10 January (lag = −29 to −14), with a maximum value of 90 m s^{-1} on 8 January. Albers and Birner (2014) showed that the enhanced westerlies in the stratosphere during lag = −20 to −10 are the general characteristics of vortex-split

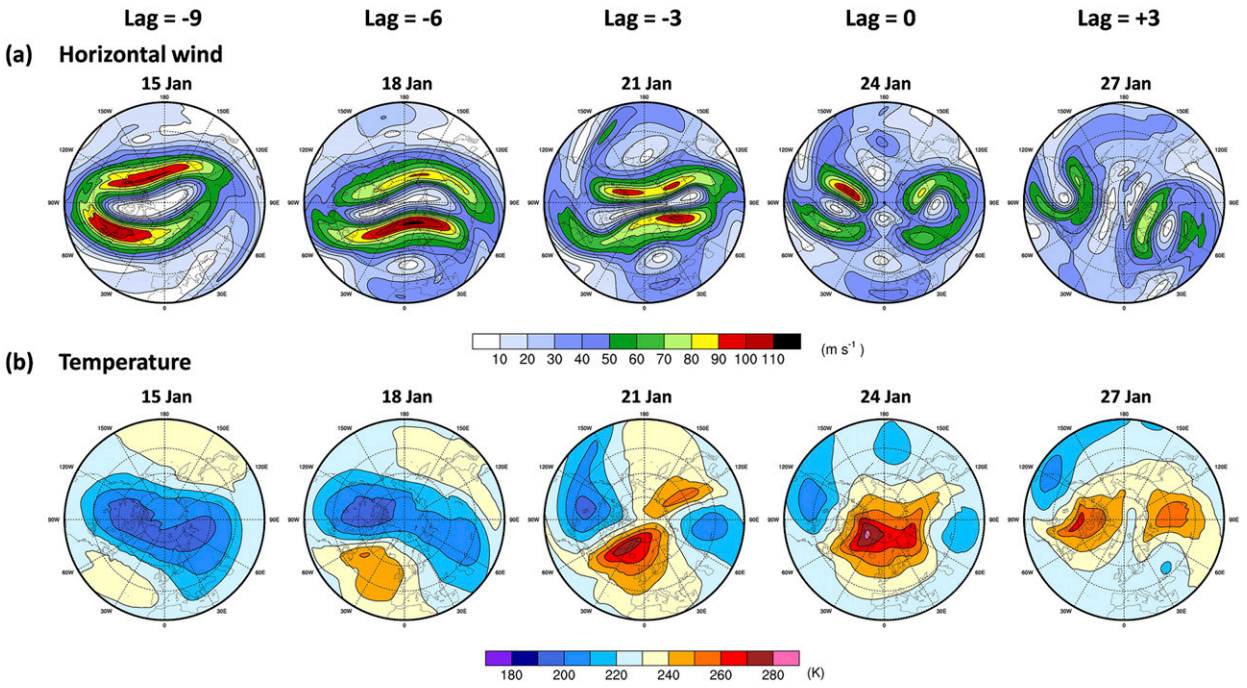

FIG. 1. Polar stereographic projection maps of the (a) horizontal wind speed and (b) temperature at 10 hPa from 15 to 27 Jan 2009 (corresponding to lag = −9 to lag = +3 when the central date of SSW is defined as lag = 0). The longitudinal (latitudinal) grid lines are drawn with dotted lines every 30° (15° starting from 30°N).

type SSWs, which can play a major role in the GWD by modifying the amount of upward-propagating GWs. As lag = 0 is approached, the westerlies gradually decrease, and their sign is reversed to easterly, starting from the lower mesosphere on 20 January (lag = −4). A rapid temperature increase of more than 30 K (Fig. 2d) occurs in the upper stratosphere starting from lag = −5 (19 January 2009), accompanied by the sudden deceleration of the polar night jet (PNJ). Although the period of sudden increase in the temperature anomalies generally coincides with that of a sudden decrease in the PNJ, the temperature increase starts earlier (from 10 January) in a shallow layer near z = 50 km, just above the cold anomalies between z = 20 and 40 km. The temperature above approximately 55 km is cold throughout the whole considered period, which becomes even colder after lag = 0.

Mesospheric cooling accompanied by stratospheric warming is a well-known phenomenon (Matsuno 1971). The vertical structure of temperature in the upper stratosphere and mesosphere during SSW09 was reported by Coy et al. (2011). Recent work by Zülicke et al. (2018) demonstrated that vertical coupling in the polar cap temperature between the stratosphere and mesosphere is approximately 70% in major SSW cases, mainly by deep zonal-mean easterlies at 60°N, which guides GW propagation in the middle atmosphere. Since Holton (1983), the mesospheric cooling has been attributed to the GWD. The deceleration of the westerly jet in the stratosphere during SSWs allows more propagation of GWs with eastward phase speeds into the mesosphere, and the resultant eastward GWD induces equatorward mass flow, resulting in the upward motion and adiabatic cooling in the polar mesosphere. However, PWs are also expected to somehow affect the mesospheric temperature during SSWs through direct momentum forcing due to upward-propagating PWs (e.g., Matsuno 1971) or PW generation due to zonally asymmetric distributions of GWs (e.g., Smith 2003). Yet, it is likely that relative roles of GWs and PWs in the change of thermal structure in the mesosphere still remain uncertain and can substantially depend on individual SSW events (Siskind et al. 2010).

b. *PW activities during SSW09*

Figure 3 shows time–latitude cross sections of the amplitudes of the geopotential height perturbations of ZWN-1 (Fig. 3a) and ZWN-2 (Fig. 3b) at four specific heights (0.1, 1, 3, and 10 hPa) and their anomalies from the daily climatology (Figs. 3c,d), which are superimposed on the zonal-mean zonal wind in Figs. 3a and 3b. Several interesting features are found from this figure. First, the amplitude of ZWN-1 is large before 21 December at most heights except at 0.1 hPa (Fig. 3a), with a statistically significant anomaly amplitude at 90% confidence level (Fig. 3c), while it suddenly weakened from 31 December to the end of January over 50°–80°N. Second, the amplitude of ZWN-2 is much weaker than that of ZWN-1 before 31 December (Fig. 3b). Third, rapid enhancement of ZWN-2 starts from 14 January with statistically significant anomaly amplitudes at 95% confidence level. The large positive anomaly amplitude of ZWN-2 at 1 hPa is diminished around 20 January, while that at 10 hPa is sustained until the end of January around 40°–70°N. Fourth, the amplitudes of PWs of ZWN-1 and ZWN-2 at 0.1 hPa are much smaller than those at lower levels, especially for ZWN-2, because PNJ controls the

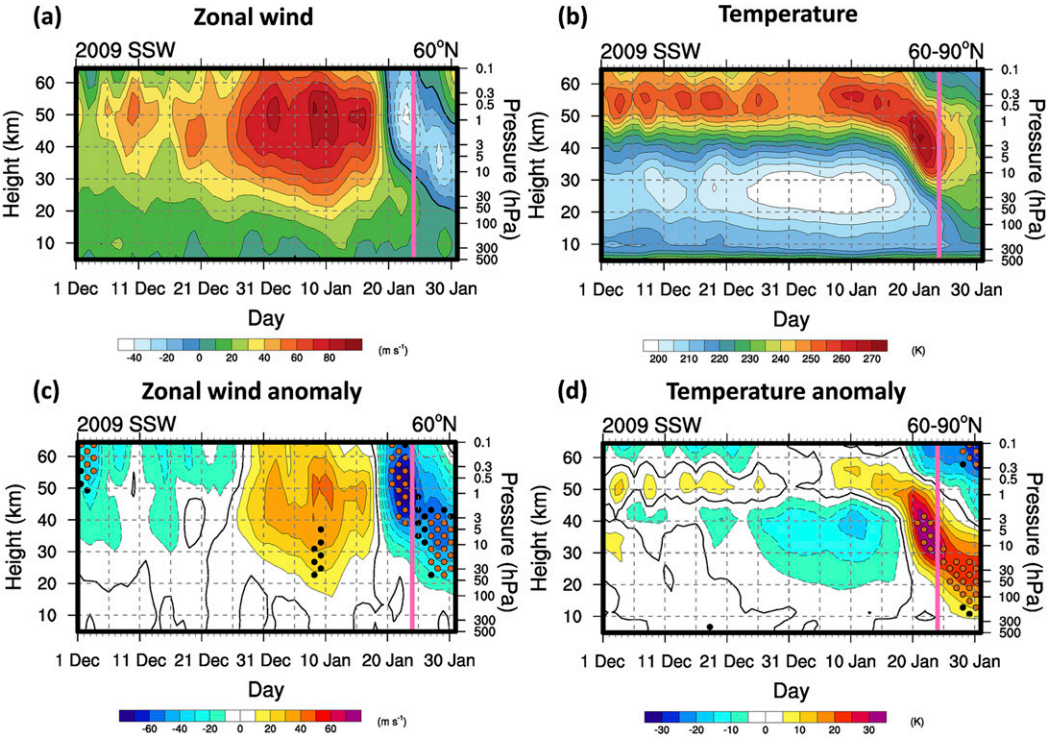

FIG. 2. Time–height cross sections of the daily averaged (a) zonal wind at 60°N and (b) polar-cap (60°–90°N)-averaged temperature during the evolution of the 2009 SSW event. (c),(d) As in (a) and (b), respectively, but for the anomalies from the 36-yr (1980–2015) climatological mean of each day. The black and brown dots in (c) and (d) denote the region where the anomalies are statistically significant for the 90% and 95% confidence level, respectively. The pink solid lines denote the central date of the 2009 SSW event (lag = 0; 24 Jan 2009).

propagation of PWs in the middle atmosphere. The PNJ maximum located at approximately 1 hPa (see Figs. 2a and 3a) causes PWs to propagate toward lower latitudes or to dissipate under the PNJ (Andrews et al. 1987), resulting in weaker PW activity at 0.1 hPa than below that level.

Figure 4 shows time–height cross sections of the amplitudes of the geopotential height perturbations of ZWN-1 and ZWN-2 at 65°N (Figs. 4a,b) and their anomalies (Figs. 4c,d) from the 36-yr (1980–2015) daily climatology during the evolution of SSW09. In addition, the evolutions of the amplitudes of ZWN-1 and ZWN-2 at 10 hPa, along with the daily climatology and plus and minus one standard deviation, are shown in Figs. 4e and 4f, respectively. The latitude of 65°N is where the maximum enhancement of ZWN-2 and decrease in ZWN-1 appear in Fig. 3. The amplitude of ZWN-1 (Figs. 4a,c) is enhanced above approximately $z = 30$ km for nearly 3 weeks from 1 to 21 December, while it decreases significantly at most altitudes above approximately $z = 20$ km from 31 December to the end of January. It seems that the increase/decrease in the amplitude of ZWN-1 above $z = 20$ km is not strongly related to that below (Fig. 4c), while the vertical connection is more evident for ZWN-2 (Figs. 4b,d) with relatively strong positive anomalies below $z = 40$ km before 21 December. At lag = −5, the amplitude of ZWN-2 in the stratosphere is significantly enhanced (Fig. 4d) with the maximum geopotential height anomaly of higher than 900 m at $z = 35$–50 km (5–1 hPa), which is statistically significant at 95% confidence level. The enhanced ZWN-2 from lag = −5 above 5 hPa is not sustained for long after lag = 0, while that below approximately $z = 20$ km remains until the end of January (Fig. 4d).

The 36-yr daily mean amplitude of ZWN-1 (Fig. 4e) at 10 hPa and 65°N calculated from the MERRA-2 data from 1 December to 31 January is approximately 900 m, which is significantly larger than that of ZWN-2 (Fig. 4f), which is approximately 300 m. Considering that the 36-yr mean includes years of SSW occurred, an approximately 600 m difference in the amplitude between ZWN-1 and ZWN-2 is quite significant. Given that the amplitude of ZWN-1 is generally predominant in the high-latitude winter stratosphere (Andrews et al. 1987; Matsuno 1970; McDonald et al. 2011; Pancheva et al. 2009), a larger amplitude of ZWN-2 than ZWN-1 during the evolution of SSW09 and other type-2 (or vortex-split type) SSWs is a distinctive phenomenon. The amplitude of ZWN-1 for SSW09 is significantly larger than the climatological mean before 27 December and is larger than one standard deviation before 18 December. However, after 28 December, the amplitude of ZWN-1 is less than the climatological mean and is continuously less than one standard deviation after 30 December. On 12 January, the amplitude of ZWN-1 is even less than two standard deviations, as also denoted by a brown dot at 10 hPa in Fig. 4c. In contrast, the amplitude of ZWN-2 for SSW09 is in the range of plus and minus one standard deviation before

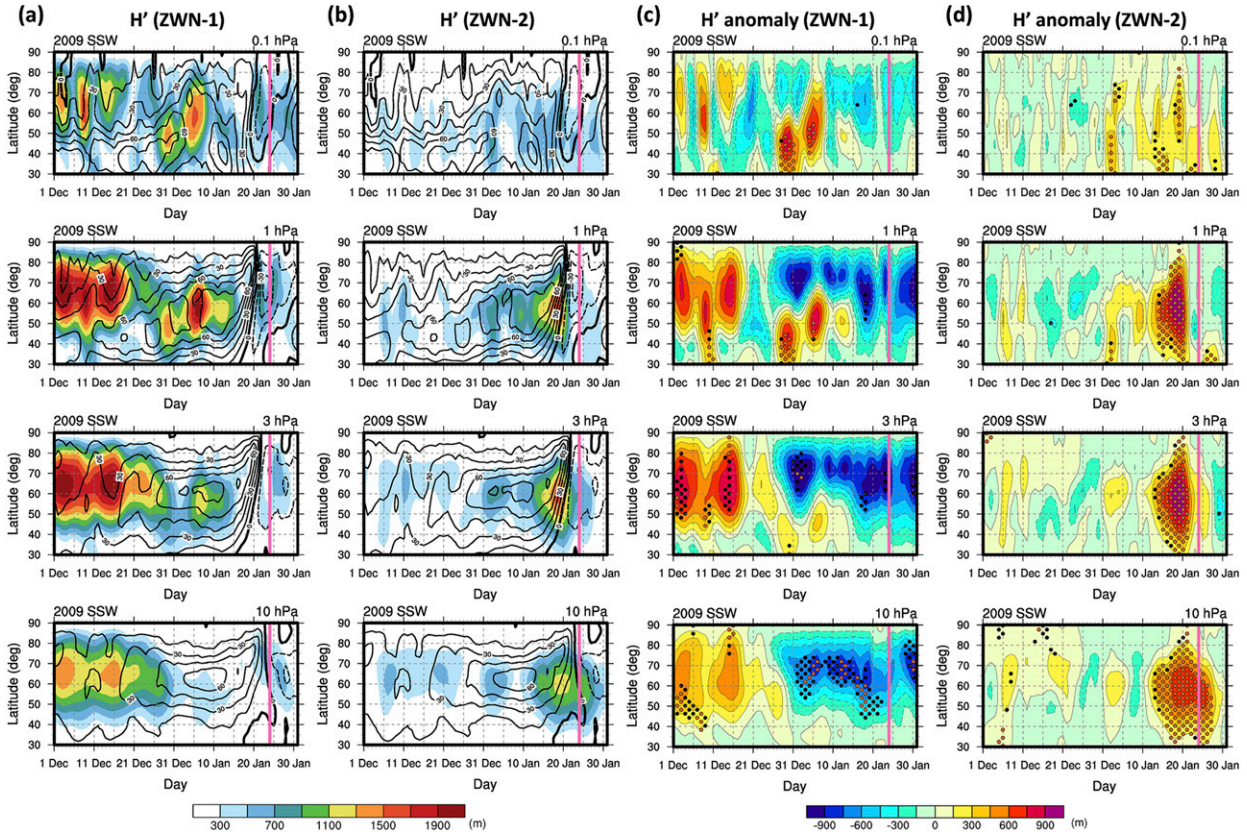

FIG. 3. Time–latitude cross sections of the daily averaged amplitudes of the geopotential height perturbations of zonal wavenumbers (a) 1 and (b) 2 at (top to bottom) 0.1, 1, 3, and 10 hPa calculated using the MERRA-2 dataset. (c),(d) As in (a) and (b), respectively, but for the anomalies from the 36-yr (1980–2015) climatological mean of each day. Zonal-mean zonal winds are overplotted with black contours in (a) and (b). The black and brown dots in (c) and (d) denote the regions where the anomalies are statistically significant for the 90% and 95% confidence level, respectively. The pink solid lines denote the central date of the 2009 SSW event (lag = 0; 24 Jan 2009).

13 January, while the amplitude increases rapidly between 13 and 27 January. In fact, the amplitude of ZWN-2 at 10 hPa is even larger than two standard deviations during 14–26 January, which is also denoted by brown dots in Fig. 4d.

PWs can deposit their momentum to the zonal-mean zonal wind when they are breaking, which is best represented by the EPD in the TEM equation. In Fig. 5, the evolution of the PW forcing during the pre-SSW period of SSW09 is examined through the EP fluxes and EPD at lag = −25, −15, and −5 by all waves, ZWN-1, and ZWN-2, respectively. The zonal-mean zonal wind at each time is overlaid in the left panels. The EP fluxes and EPD at lag = −25 (31 December 2008) by all waves are similar to those of the daily climatology on 31 December (not shown). The contribution by ZWN-2 to the total EPD is larger than that by ZWN-1 at lag = −15, and it becomes predominant at lag = −5 with a maximum magnitude of 116 m s^{-1} day^{-1} at 0.1 hPa, which is more than 90% of the total EPD. In fact, EP flux and EPD at lag = −5 are significantly larger than those at the previous times, mainly by ZWN-2, which is responsible for the zonal-mean zonal wind reversal at 0.1 hPa, as shown in Fig. 2a. Note that the contribution of PWs with ZWN ≥ 3 to the total EPD is negligibly small (not shown) at lag = −25, −15, and −5, implying that the EPD represents mostly forcing by PWs of ZWN-1 and ZWN-2, without significant contribution by resolved GWs, which is somewhat different from the result of Sato and Nomoto (2015) where EPD by resolved GWs, which was defined by ZWN ≥ 4, is significant in the mid- to high latitudes of winter mesosphere.

c. *Contribution of GWD during the evolution of SSW09*

Figure 6 shows the latitude–height cross sections of the zonal wave forcing induced by all resolved PWs (EPD), the zonal component of parameterized GWD (GWD_X), and the contribution of GWD_X to the total wave forcing (EPD + GWD_X). The residual mean velocity vector ($\bar{v}^*$, $\bar{w}^*$) induced by EPD and GWD_X is overlaid on Figs. 6a and 6b, respectively. Each wave forcing is averaged between lag = −30 and lag = −5. A negative EPD forcing (Fig. 6a) exists in most regions, except near z = 50–60 km and 60°–70°N where a localized positive EPD forcing exists, which is likely due to the positive EPD in the lower mesosphere near 50°–70°N at lag = −25 and near 55°–80°N at lag = −15 shown in Fig. 5a. The negative EPD forcing in the mid–high-latitude stratosphere can induce direct residual mean circulation in the NH (Andrews et al. 1987;

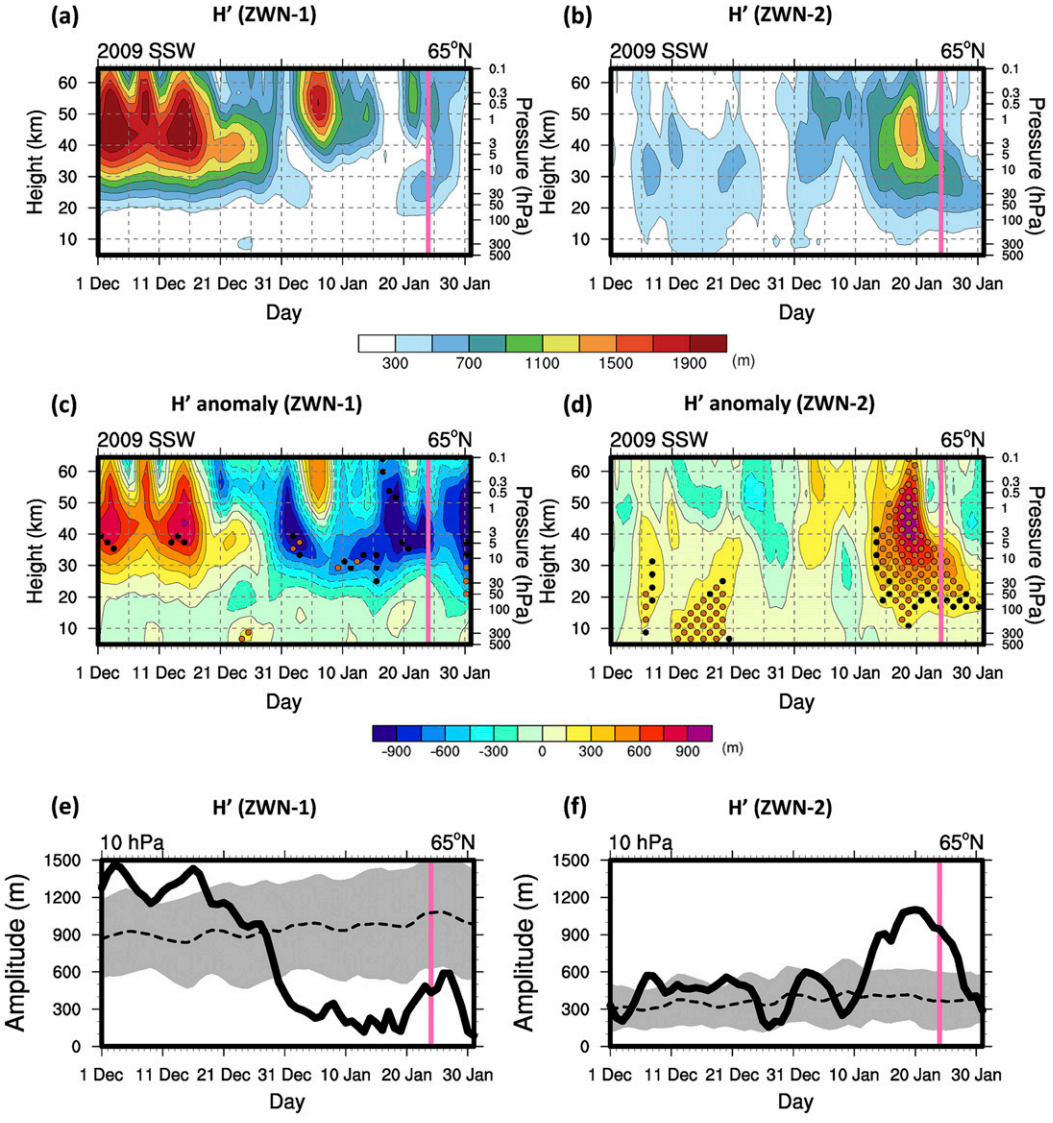

FIG. 4. Time–height cross sections of the daily averaged amplitudes of the geopotential height perturbations of zonal wavenumbers (a) 1 and (b) 2 at 65°N during the evolution of the 2009 SSW event. (c), (d) As in (a) and (b), respectively, but for the anomalies from the 36-yr (1980–2015) climatological means, which are shown as dashed lines in (e) and (f), respectively. The shading in (e) and (f) represents ±1 standard deviation and thick solid lines denote wave amplitude for SSW09 case. The black and brown dots in (c) and (d) denote the regions where the anomalies are statistically significant for the 90% and 95% confidence level, respectively. The pink solid lines denote the central date of the 2009 SSW event (lag = 0; 24 Jan 2009).

Cohen et al. 2014; Song and Chun 2016; Martineau et al. 2018), resulting in adiabatic warming in the polar region by the downdraft (negative $\overline{w}^*$). The general features of the EPD during the pre-SSW period are well presented in the SSW09 case, albeit with a much larger magnitude than for other SSW cases (Harada et al. 2010; Harada and Hirooka 2017). The positive EPD near $z = 50$–60 km and 60°–70°N shown in Fig. 6a is somewhat interesting, and we have checked whether this is similar to the eastward-propagating traveling PWs generated in situ through the baroclinic instability processes, which was proposed by Sato and Nomoto (2015). We found that there exists some similarities and difference between the current results and those from Sato and Nomoto (2015), which will be discussed in the last section (with Fig. 17).

The GWD forcing is negative in the pre-SSW period (Fig. 6b), mostly above 10 hPa with a maximum magnitude of 38 m s^{-1} day^{-1} at 0.1 hPa, 70°N and a secondary maximum of 3.4 m s^{-1} day^{-1} at 4 hPa, 66.5°N. Clarifying the sources of GWs is not straightforward given that the parameterized GWD used in this study is the sum of the orographic and nonorographic GWs. However, one aspect that is clear is that the GWD schemes used for MERRA-2 are based on the

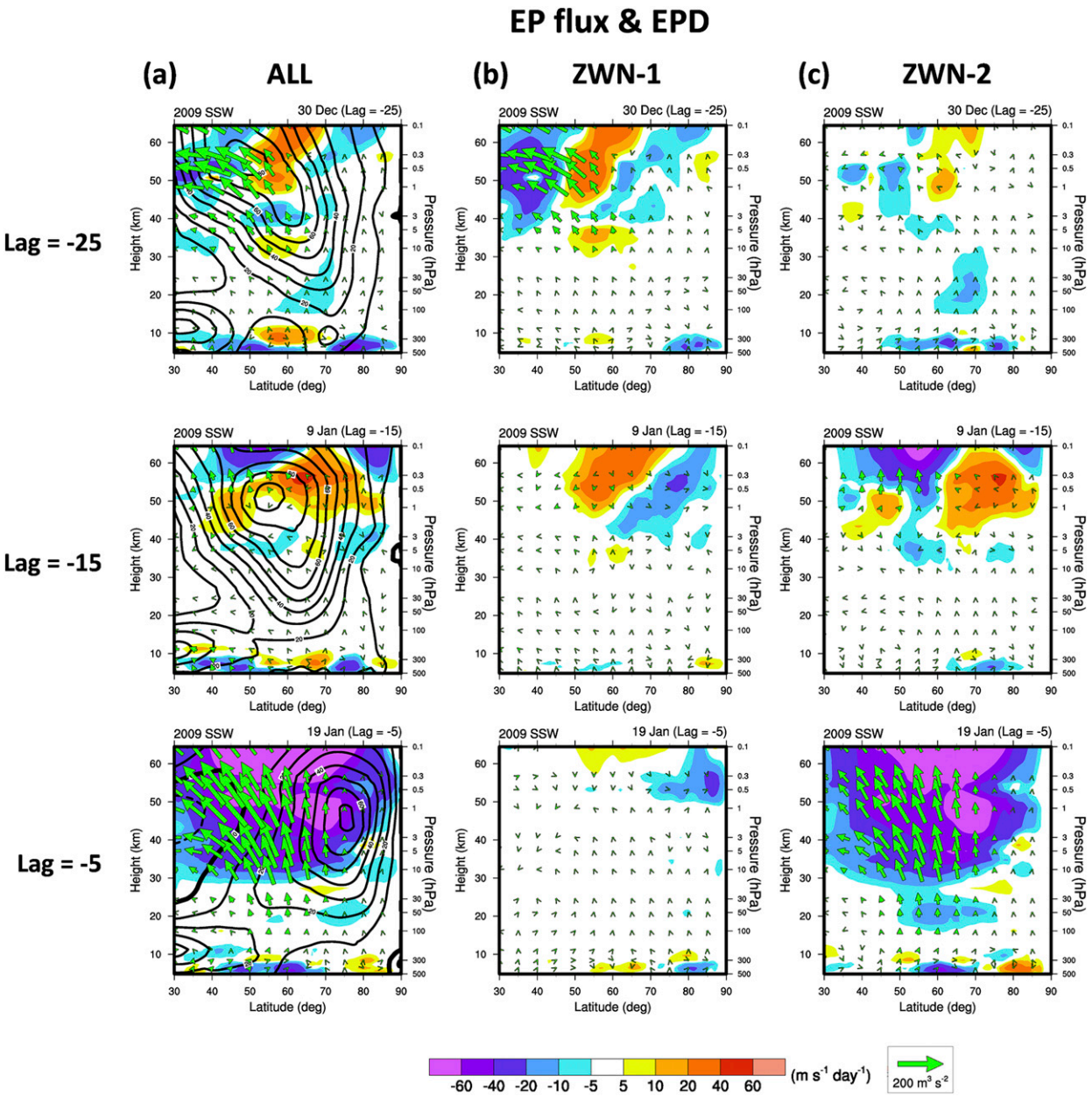

FIG. 5. Latitude–height cross sections of the Eliassen–Palm fluxes (EP fluxes; green vectors) and their divergences (EPD; shading) at lag = (top) −25, (middle) −15, and (bottom) −5 by (a) all waves, (b) zonal wavenumber 1, and (c) wavenumber 2. The zonal-mean zonal wind is contoured by solid lines for westerlies and dashed lines for easterlies. For better visualization, $F^{(\phi)}$ and $F^{(z)}$ are multiplied by $\cos\phi/(\rho_0 a\pi)$ and $\cos\phi/(\rho_0 10^5)$, respectively.

columnar propagation for both orographic and nonorographic GWs, as in most current GWD schemes (Kim et al. 2003), and the strong negative GWD_X in 50°–80°N is likely mostly from nonorographic GWs, considering that major mountains exist near 30°–50°N in the NH. A weak GWD_X in the low stratosphere near z = 15–25 km at 30°–50°N (Fig. 6b) is likely due to orographic GWs, given that large-amplitude orographic GWs break easily at low altitude, resulting in a relatively weak GWD due to the large density there. The strong negative GWD_X above z = 60 km stems from both nonorographic GWs and relatively weak orographic GWs that could survive to the mesosphere before breaking. The residual mean vertical velocities induced by GWD_X are predominantly negative, with the maximum magnitude in the lower mesospheric layer between 0.3 and 0.1 hPa over 75°–85°N and the secondary maximum in the upper stratospheric layer between 10 and 3 hPa at 70°N. The adiabatic warming by the downdrafts concentrated in 60°–85°N can contribute to the warming of SSW09, as shown

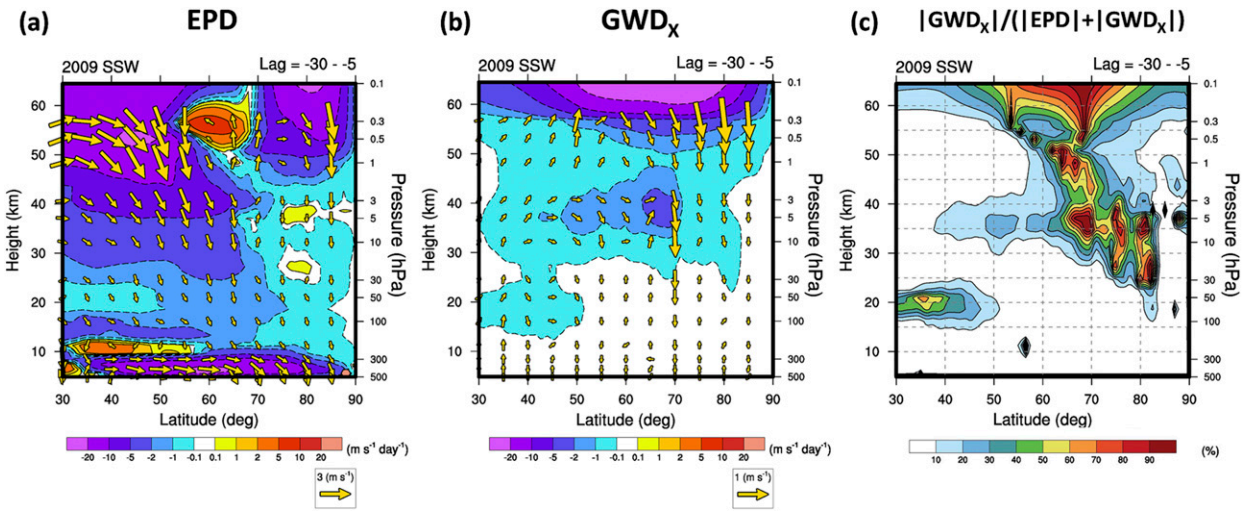

FIG. 6. Latitude–height cross sections of the (a) Eliassen–Palm flux divergence (EPD) by all resolved waves, (b) zonal gravity wave drag (GWD_X), and (c) the percentage of GWD_X to the total wave forcing ($|EPD| + |GWD_X|$) averaged between lags = −30 and −5 (25 Dec 2008 and 19 Jan 2009). The residual mean velocity vector ($\overline{v}^*$, $\overline{w}^*$) induced by EPD (GWD_X) calculated using Eqs. (7) and (8) is overlaid in (a) [(b)]. For better visualization, $\overline{w}^*$ is multiplied by 333 in the residual mean velocity vector shown in (a) and (b).

in Figs. 1 and 2. Although GWD_X is mostly smaller than EPD except in the upper stratosphere, the ratio of GWD_X to the total wave forcing (Fig. 6c) is up to 90% at some latitudes and heights during the pre-SSW period of SSW09, such as 65°–80°N, 10–3 hPa and 60°–70°N over 0.3 hPa. This demonstrates the importance of GWs in SSW, which is consistent with the work by Albers and Birner (2014) based on the composite analysis including all SSW events that occurred during 1980–2011.

Figure 7 shows the GWD_X superimposed on the zonal-mean zonal wind (Fig. 7a) and their anomalies (Fig. 7b) from the daily climatology at 70°N. Here, 70°N is selected as the magnitude of the negative GWD_X (Fig. 6b) and the GW contribution to the total wave forcing (Fig. 6c) were at their maxima there. Temporal and vertical distributions of GWD_X (Fig. 7a) show (i) predominant negative values in the lower mesosphere at most times before 20 January, with larger magnitudes from mid-December to mid-January, (ii) negative values in the stratosphere above 10 hPa from mid-December to mid-January, although with much smaller values than in the upper mesosphere, and (iii) a sign reversal (from negative to positive) at lag = −3, starting from the lower mesosphere and extending down to the upper stratosphere (3 hPa) until 31 January. In the GWD_X anomaly field (Fig. 7b), the westward GWD is weaker (positive anomaly) before 19 December 2008, mostly above 0.3 hPa, while it is stronger (negative anomaly) between 19 December 2008 and 19 January 2009 than the daily climatology, mostly above 10 hPa; the exception is on 28 December 2008, where the anomaly extends down to $z = 10$ km. Given that the sign of GWD_X is proportional to the sign of GW momentum

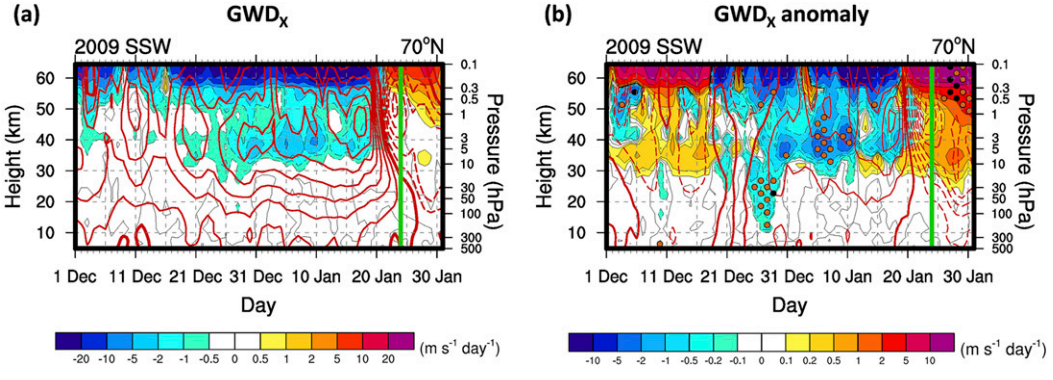

FIG. 7. Time–height cross sections of (a) zonal GWD (GWD_X) and (b) its anomaly from the 36-yr (1980–2015) climatological mean for each day at 70°N. Zonal-mean zonal wind and their anomaly at 70°N are superimposed with red contours in (a) and (b), respectively. The contour interval is 10 m s^{-1}, with negative values dashed. The black and brown dots denote the regions where the anomalies are statistically significant for the 90% and 95% confidence level, respectively. The green solid lines denote the central date of the 2009 SSW event (lag = 0; 24 Jan 2009).

flux (Lindzen 1981), which is determined by the sign of $c–U$ (where c is the GW phase speed and U is the background wind), the large negative GWD_X shown in Fig. 7 is likely due to the dissipation of GWs with phase speeds less than the westerly background wind speed, either through critical-level filtering under strong wind shear or wave breaking. The positive GWD_X after 20 January can be explained by the same mechanism except for the nonorographic GWs with phase speeds larger than the easterly background wind (i.e., negative background wind). It is interesting that statistically significant anomalies at 90% and 95% confidence level denoted by black and brown dots, respectively, exist more in the middle stratosphere than in the lower mesosphere, although the magnitude of enhanced negative GWD_X is much larger in the lower mesosphere. The extremely strong GWD_X in the stratosphere during SSW09, including the lower to midstratosphere below 10 hPa during 25–29 December and the mid- to upper stratosphere during 5–10 January, is quite unique, which is ideal for studying the contribution of GWs to SSW.

The period of the negative (positive) GWD_X anomaly is generally matched to that of the positive (negative) zonal-mean zonal wind anomaly centered near 1 hPa (Fig. 7b). The impacts of the zonal-mean zonal wind on the magnitude of GWD_X in the middle atmosphere are not straightforward and depend on both the phase speed spectrum of GW sources and the dominant wave dissipation process (wave breaking or critical-level filtering). Note again that the GWD provided from MERRA-2 is based on the columnar GWD parameterization schemes, exclusively allowing for the vertical propagation of GWs, and thus, the horizontal wavenumbers and frequency (and horizontal phase speed) cannot be changed during wave propagation. Under this restriction, a strong background wind is not a favorable condition for wave breaking for an orographic GW (Lindzen 1981; Andrews et al. 1987). For nonorographic GWs with a wide phase speed spectrum, strong wind shear associated with PNJ, rather than the magnitude of PNJ, may be positively correlated with the magnitude of GWD in the stratosphere through the critical-level filtering process. Several previous studies have shown that high stratospheric wind speeds correspond to increased GWD in the winter stratosphere (McLandress et al. 2000; Venkat Ratnam et al. 2004; Wang and Alexander 2009) as well as for vortex-split SSW events (Albers and Birner 2014; Song and Chun 2016), which is consistent with the current result (Fig. 7b). In contrast, the GWD for vortex-displacement SSW events is anomalously weakened for a strong PNJ period (Albers and Birner 2014; Song and Chun 2016).

To check the robustness of GWD in the MERRA-2, we used the total wind tendency due to model physics provided by the ECMWF Coupled European Reanalysis of the Satellite Era (CERA-SAT) (Schepers et al. 2018) forecasts made using the ECMWF Integrated Forecasting System (IFS) model Cy42r1 with nonorographic GWD scheme (Scinocca 2003). The total wind tendency can be assumed to be almost same as GWD in the stratosphere (Albers and Birner 2014) considering the negligible wind tendencies by turbulence or moisture physics in the middle atmosphere. The total physics tendencies retrieved on 137 model levels with a horizontal resolution of 0.5° × 0.5° are used. For the analysis of PWs and mean flows, winds and temperature in the MERRA-2 are used because the USLM of the MERRA-2 where *Aura* MLS data are assimilated (Gelaro et al. 2017) can be more realistic compared with the ECMWF CERA-SAT. All variables on the model levels are interpolated at 47 pressure levels up to 0.01 hPa (~80.6 km). We used the mean of 10 ensemble members for analysis. Some similar results are found in CERA-SAT. First, the enhanced westward GWD during prestage of SSW09 and their sign reversal around the central date of SSW09 appear at approximately 0.1 hPa (Figs. S1a,b in the online supplemental material). The characteristics of GWD in CERA-SAT as a possible source of PW generation will also be compared with MERRA-2 in the following section.

4. Nonconservative GWD forcing in the QGPV equation

To investigate the role of GWD on PW generation, a linearized disturbance QGPV equation in log-pressure coordinates is considered (Andrews et al. 1987):

$$\left(\frac{\partial}{\partial t}+\overline{u}\frac{\partial}{a\cos\phi\partial\lambda}\right)q'+v'\frac{\partial\overline{q}}{a\partial\phi}=\frac{1}{a\cos\phi}\left[\frac{\partial Y'}{\partial\lambda}-\frac{\partial(X'\cos\phi)}{\partial\phi}\right]+\frac{f_o}{\rho_o}\frac{\partial}{\partial z}\left[\rho_o\frac{Q'}{e^{(\kappa/H)z}\left(\frac{\partial\overline{T}_o}{\partial z}+\frac{\kappa\overline{T}_o}{H}\right)}\right], \tag{9}$$

$$q'\equiv\frac{1}{a^2\cos\phi}\left[\frac{1}{\cos\phi}\frac{\partial^2}{\partial\lambda^2}+\frac{\partial}{\partial\phi}\left(\cos\phi\frac{\partial}{\partial\phi}\right)\right]\psi'+\frac{1}{\rho_o}\frac{\partial}{\partial z}\left(\rho_o\frac{f_o^2}{N^2}\frac{\partial\psi'}{\partial z}\right), \tag{10}$$

$$\frac{\partial\overline{q}}{a\partial\phi}\equiv\frac{2\Omega\cos\phi}{a}-\frac{1}{a^2}\frac{\partial}{\partial\phi}\left[\frac{1}{\cos\phi}\frac{\partial(\overline{u}\cos\phi)}{\partial\phi}\right]-\frac{1}{\rho_o}\frac{\partial}{\partial z}\left(\rho_o\frac{f_o^2}{N^2}\frac{\partial\overline{u}}{\partial z}\right). \tag{11}$$

Here, q' is the perturbation QGPV, $\overline{u}$ is the zonal-mean zonal wind, v' is the perturbation meridional wind, $\overline{q}$ is the zonal-mean QGPV, X' and Y' are the perturbation zonal (GWD'_X) and meridional (GWD'_Y) components of GWD, respectively, Q' is the perturbation diabatic heating rate, $\overline{T}_o$ is zonal-mean reference temperature defined as the monthly averaged value, ψ' is the perturbation streamfunction ($\psi'=\Phi'/f_o$, where Φ' is the perturbation geopotential), and λ is longitude. The two bracketed terms on the right-hand side of (9) are so-called the nonconservative forcing terms of QGPV (Andrews et al. 1987), which are associated with the momentum forcing by small-scale waves such as GWs and diabatic heating effect, respectively. Although the nonconservative forcing terms have been ignored in most previous studies, it is worth investigating whether the nonconservative GWD forcing defined by Z' below, the terms in the first bracket on the right-hand side of (9), is related to the rapid enhancement of PWs before the onset of the SSW09 event:

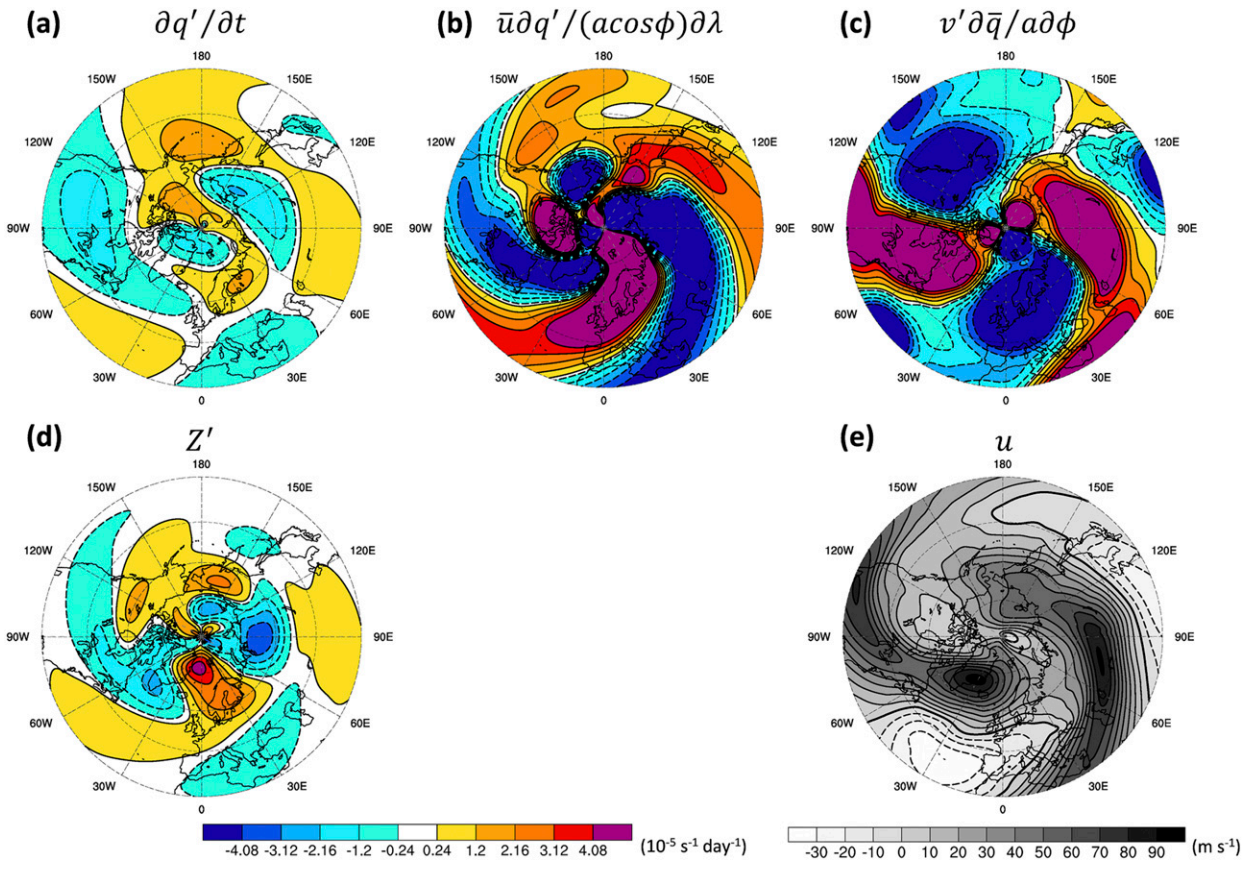

FIG. 8. Polar stereographic projection maps of the (a) tendency of QGPV perturbation ($\partial q'/\partial t$), (b) zonal advection of q', (c) meridional advection of planetary potential vorticity, (d) nonconservative GWD forcing (Z') of Eq. (9), and (e) zonal wind averaged over 0.3–0.1 hPa at lag = −6 (18 Jan 2009). For each variable, the components with zonal wavenumbers 1–3 are used in (a)–(d) for clarity, and a polar stereographic projection map is plotted from 30°N to the North Pole with an interval of 15° latitude.

$$Z' = \frac{1}{a\cos\phi}\left[\frac{\partial Y'}{\partial\lambda} - \frac{\partial(X'\cos\phi)}{\partial\phi}\right]. \tag{12}$$

We first examine whether the NCGWD forcing term (Z') is nonnegligible compared with other terms in (9). Figure 8 shows the first four terms in (9): (Fig. 8a) $\partial q'/\partial t$, (Fig. 8b) $\bar{u}\partial q'/(a\cos\phi)\partial\lambda$, (Fig. 8c) $v'\partial\bar{q}/a\partial\phi$, and (Fig. 8d) Z', along with (Fig. 8e) zonal wind averaged over 0.3–0.1 hPa at lag = −6. The vertical height range and time shown in Fig. 8 are selected, as GWD_X is maximum at 0.3–0.1 hPa (Fig. 7) and the anomalous ZWN-2 at 10 hPa, where the PW amplitude associated with SSW is evaluated, is maximum at lag = −6 (Fig. 4f). In the calculation of each term in (9), large-scale components with ZWNs 1–3 are used exclusively. We found that there is no significant difference in Z' when all ZWN components of GWD_X and GWD_Y are considered (not shown). Several interesting features are found in Fig. 8. First, the zonal advection of perturbation PV by the mean flow (Fig. 8b) and meridional advection of mean PV by the perturbation wind (Fig. 8c) are the two major terms, which are concentrated along the two spiral PNJs that extended down to the lower latitudes (Fig. 8e). Second, the major two terms (Figs. 8b,c) largely canceled each other, and consequently, the local tendency of the perturbation PV is much weaker than the two major terms. Third, Z' is similar to $\partial q'/\partial t$ in its magnitude and phase poleward of approximately 30°N, with a clear ZWN-2 structure at 50°–80°N. The pattern correlation coefficients between Z' and $\partial q'/\partial t$ are 0.47 and 0.64 at 50°–80°N and 40°–60°N, respectively. These correlation coefficients are statistically significant at 95% confidence level when effective spatial degrees of freedom (Wang and Shen 1999) is considered. This result demonstrates that the NCGWD forcing in the lower mesosphere is nonnegligible and can play an important role in determining the ZWN-2 structure PWs through the tendency of q'. Note that the magnitude of nonconservative forcing by the diabatic heating rate and analysis increment is about 15 times and 3 times smaller than Z', respectively.

a. Relationship between PWs and the NCGWD during SSW09

To understand the relationship between PWs and the NCGWD forcing term simultaneously during the evolution of SSW, longitude–height cross sections of Z' and geopotential height perturbations (H') averaged over 50°–80°N from 12 (lag = −12) to 27 January 2009 (lag = +3) are shown in Fig. 9. Note that the NCGWD forcing and geopotential

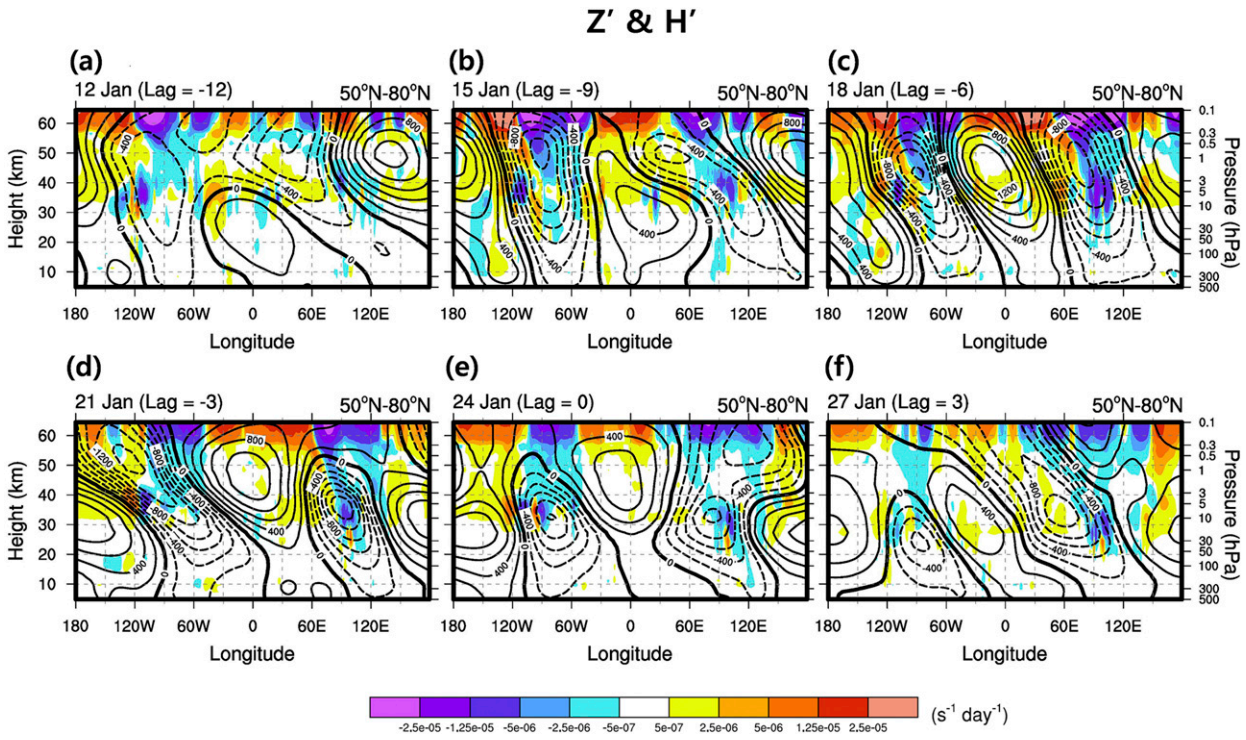

FIG. 9. Longitude–height cross sections of Z' (shading) and geopotential height perturbations (H') (contours) averaged over 50°–80°N from 12 to 27 Jan 2009 (corresponding to lag = −12 to lag +3).

height perturbation shown in Fig. 9 include all PW components, unlike in Fig. 8, where ZWNs 1–3 are used exclusively. At lag = −12, the ZWN-2 pattern of PW is not clear in the stratosphere (Fig. 9a), whereas they are predominant in the mid- to upper stratosphere from lag = −9 to lag = 0 (Figs. 9b–f). After lag = 0, the ZWN-2 pattern of PW diminishes (Fig. 9f) in the lower mesosphere, while it still remains in the mid-stratosphere. The ZWN-2 pattern of the Z' is developed between lag = −9 and lag = −3, especially in the lower mesosphere (at 0.3–0.1 hPa), with the secondary maximum at approximately 5 hPa. Although the ZWN-2 structure of Z' was already shown in Fig. 8d at 0.3–0.1 hPa and lag = −6, the predominant ZWN-2 pattern of Z' in the lower mesosphere and stratosphere is somewhat unexpected, considering the relatively localized GWD forcing in the middle atmosphere and even more localized NCGWD forcing term that involves horizontal derivatives of the zonal and meridional components of GWD. For the NCGWD forcing to generate PWs of ZWN-2 in the linearized QGPV equation [Eq. (9)], the ZWN-2 pattern of the forcing is generally required, as for any linearized forced wave equation. At lag = +3, there is no coherent zonal structure of Z' in the whole stratosphere.

The relative importance in the ZWN-2 components of the NCGWD forcing during the evolution of SSW09 is further examined through spectral analysis. Figure 10a shows the temporal variations in the power of Z' averaged over 50°–80°N and 0.3–0.1 hPa with respect to the zonal wavenumber. Except for a short period before 6 December, where the largest power exists at ZWN-1, the ZWN-2 structure of Z' is predominant, with three peak times on 6–21 December, 31 December–8 January, and 15–20 January. These three periods are generally matched with those of the positive anomaly of ZWN-2 at 65°N, as shown in Figs. 4d and 4f. It is interesting that although the power of the ZWN-2 component of Z' is larger during the first period (6–21 December) than during the third period (15–20 January), the amplitude of PW of ZWN-2 (see Fig. 4) is larger in the third period than in the first period. The enhanced ZWN-2 component of Z' can be found in other vortex-split type SSW cases, such as the January 1985 SSW event (not shown), which is accompanied by enhanced PWs with ZWN-2 during the pre-SSW period.

To examine whether the ZWN-2 structure of NCGWD forcing exists at other altitudes, a time–height cross section of the amplitude of the ZWN-2 component of Z' during SSW09 evolution is shown in Fig. 10b. The ZWN-2 structure of Z' is predominant in the lower mesosphere (0.3–0.1 hPa), with the secondary maximum in the midstratosphere (10–3 hPa), which is expected from the magnitudes of GWD_X (Fig. 7) and Z' (Fig. 9). Although the magnitude is relatively small, the temporal variation in Z' at 10–3 hPa is similar to that in the lower mesosphere (0.3–0.1 hPa), with spectral peaks being matched almost simultaneously in the two layers on 5–21 December 2008, 1–9 January, and 15–21 January 2009. Considering that the rapid enhancement of PWs with ZWN-2 above the mid-stratosphere during the evolution of SSW09 (Figs. 4b,d) is well correlated with that of Z' (Fig. 10) and considering that $\partial q'/\partial t$ is almost in phase with Z' in the mid- to high latitudes of the lower mesosphere (Fig. 8), it can be postulated that PWs in the

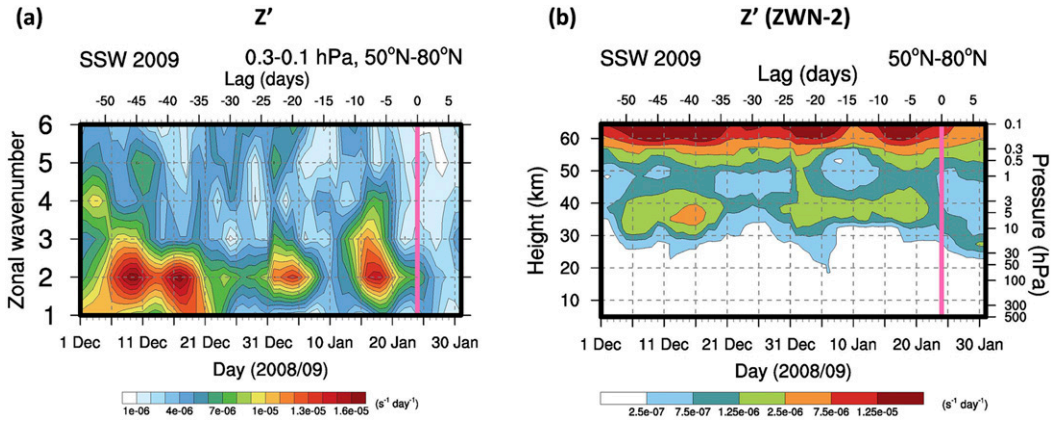

FIG. 10. (a) Time series of the amplitudes of the Z' averaged over 50°–80°N and 0.3–0.1 hPa for zonal wavenumbers (ZWN) 1–6. The running mean for a 5-day window is performed using the daily averaged values. (b) Time–height cross section of the amplitudes of Z' averaged over 50°–80°N for the ZWN-2 component. The pink solid lines denote the central date of the 2009 SSW event (lag = 0; 24 Jan 2009).

stratosphere and lower mesosphere are related to those generated by the NCGWD forcing either from higher levels or the same level. Indeed, Holton (1984) and Smith (2003) demonstrated through modeling studies the in situ generation of PWs by GWD in the winter mesosphere and the vertical spread of PWs down to the winter stratosphere.

This possibility is examined further through calculation of the correlation coefficient between the PW of ZWN-2 in the stratosphere and the NCGWD forcing in the upper stratosphere and lower mesosphere (USLM). Figure 11 shows the lag-correlation coefficients between the ZWN-2 component of Z' averaged over 30°–80°N at 0.3–0.1 hPa and the PWs (H') of ZWN-2 averaged at 30°–90°N above z = 20 km where the PWs of ZWN-2 are significantly enhanced, which is calculated using 1-month daily data from 1 to 31 January 2009. Here, a positive time lag means that Z' precedes H' of ZWN-2. Statistically significant correlations for the 95% confidence level are denoted by blue dots. The ZWN-2 component of Z' at 0.3–0.1 hPa and the PWs of ZWN-2 in the stratosphere have significant positive correlations mainly at positive time lags, indicating that the temporal variation of Z' of ZWN-2 precedes the change of H' of ZWN-2. In other words, the result shown in Fig. 11 demonstrates that the abrupt amplification of PWs of ZWN-2 in the stratosphere before the onset of SSW09 is closely related to the enhanced ZWN-2 pattern of Z' at 0.3–0.1 hPa prior to the enhanced PW of ZWN-2 in the midstratosphere. The positive correlation coefficients have peaks at the longer positive lagged times as they descend to the lower altitude. This finding implies that the enhanced ZWN-2 component of Z' in the lower mesosphere can generate the PW of ZWN-2 in the lower mesosphere, which can extend down to the midstratosphere and contribute to the enhanced PW of ZWN-2 a few days later. To clarify the possibility of the downward propagation of PWs, wave deposition is performed in the following section.

b. Decomposition of the PW of ZWN-2

To examine the possibility of downward-propagating PWs of ZWN-2 generated by Z' in the lower mesosphere, PWs of ZWN-2 are decomposed into upward- and downward-propagating components based on a 2D (zonal, time) Fourier analysis. The Fourier decomposition is carried out as follows: First, 11-day time windows moving at a 1-day interval are considered. The results of the Fourier analysis within each moving window are placed at the centers of each window. These sliding time windows cover two months (from December 2008 to January 2009), which are used to investigate the evolution of SSW09 in this study. The 11-day window can include PWs with a 2–11 day period. The 11-day windows are chosen based on the fact that PWs with periods of 4–25 days

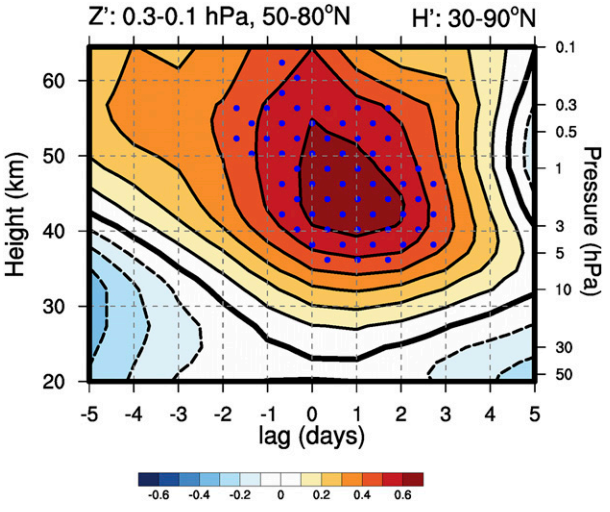

FIG. 11. Vertical distributions of time-lagged correlations of the ZWN-2 component of the amplitudes of the Z' averaged over 50°–80°N at 0.3–0.1 hPa with the amplitude of the geopotential height perturbation (H') of ZWN-2 averaged over 30°–90°N. Daily averaged values from 1 to 31 Jan 2009 are used to calculate the correlations. A positive time lag means that Z' precedes H' of ZWN-2. Statistically significant correlations for the 95% confidence level are denoted by blue dots.

exist during the NH winter season (Hirooka and Hirota 1985; Sassi et al. 2012) and that longer time windows can cause uncertainties in the wave analysis due to the rapid changes in the mean fields during the evolution of the SSW09. Especially, Kishore et al. (2012) showed that the PW with a period of about 7–11 days (7–13 days) is one of the significant PW components in the polar winter stratosphere (mesosphere) during the evolution of SSW09.

Then, the Fourier decompositions within the given time windows are conducted on the PWs for any 2D variable $f(\lambda, t)$:

$$F(k,\omega) = \left(\frac{1}{2\pi}\right)^2 \int_{-\infty}^{\infty}\int_{-\infty}^{\infty} f(\lambda,t)e^{-i(kx+\omega t)}\,d\lambda\,dt, \qquad (13)$$

where $F(k, \omega)$ is the complex coefficient with respect to a ZWN (k) and frequency (ω). $f(\lambda, t)$ can be expressed as follows by the inverse Fourier transform:

$$f(\lambda,t) = \int_{-\infty}^{\infty}\int_{-\infty}^{\infty} F(k,\omega)e^{i(kx+\omega t)}\,dk\,d\omega. \qquad (14)$$

Following Kao (1968), a covariance term consisting of the perturbations of two variables $f(\lambda, t)$ and $g(\lambda, t)$ can be expressed as follows:

$$[\overline{f'g'}] = \int_{-\infty}^{\infty}\int_{-\infty}^{\infty} \mathrm{CO}_{f',g'}(k,\omega)\,dk\,d\omega. \qquad (15)$$

Here, the mean field is defined as the zonal (overbar, $\overline{\cdots}$) and time averaged (square brackets, $[\cdots]$) value, and the perturbations are a departure from the mean field. $\mathrm{CO}_{f',g'}$ is the cospectrum of f' and g', which can be written as follows:

$$\mathrm{CO}_{f',g'} = \mathrm{Re}[F'G'^{*}], \qquad (16)$$

where F' and G' are the Fourier transforms of f' and g', respectively, and G'^{*} is the complex conjugate of G'. A 2D Fourier component consisting of a certain k and ω will have either a positive or negative zonal phase speed, depending on the sign of ω for the positive zonal wavenumber. The stationary (i.e., $c = \omega = 0$) component is also available in this analysis with 11-day windows. To investigate the evolution of the PWs of ZWN-2 during SSW09, a case with wavenumber 2 ($k = 2$; ZWN-2) is exclusively considered in the section. The vertical component of the EP flux ($F^{(z)}$) calculated based on the 2D Fourier decomposition described above is used to separate the upward ($F^{(z)} > 0$)- and downward ($F^{(z)} < 0$)-propagating components of PWs. Considering that the amplitudes of the Fourier components with high frequencies ($|\omega| \geq 2$) are relatively small (not shown), we focus on the results of the low-frequency components, including the stationary components ($|\omega| \leq 1$). The PWs of $\omega = 1$ ($\omega = -1$) correspond to the eastward (westward)-propagating wave with a period of 11 days.

The 2D decomposed geopotential height perturbations of ZWN-2 with stationary ($\omega = 0$) and $\omega = 1$ components over 50°–65°N at lag = −7 are shown in Fig. 12. The $\omega = 1$ components are chosen because of their substantial downward-propagating features in the stratosphere during the evolution of the SSW09, which is suitable for analyzing the PWs generated by the GWs in the USLM, while no apparent downward propagations are found in the PWs with $\omega = -1$ components. When we performed above mentioned 2D decomposition of PWs using a 25-day time window in addition to the currently used 11-day time window, dominant downward-propagating signals are found at periods of 12.5 and 8.3 days (not shown). This confirms that downward-propagating PWs of ZWN-2 from USLM to the stratosphere during SSW09 have a period of about 10 days.

The H's are decomposed into upward (Figs. 12b,e)- and downward-propagating (Figs. 12c,f) components based on the sign of $F^{(z)}$ within the given latitude and height ranges. For the stationary components, westward-tilted structures with a maximum amplitude of approximately 1000 m at 5–1 hPa are evident, suggesting the dominant upward propagation of PWs (see Figs. 12b,c). However, for the $\omega = 1$ components, H's have mixed structures of the upward (westward-tilted)- and downward (eastward-tilted)-propagating PWs with a maximum amplitude of approximately 240 m near 1 hPa. In particular, clear downward-propagating signals appear at 5–0.3 hPa, and the signals gradually descend to the lower stratosphere, as shown in Fig. 13, where temporal variations in the downward-propagating ZWN-2 PWs with $\omega = 1$ are presented, along with the nonconservative GWD forcing (Z') from lag = −9 to lag = −4. At lag = −9, the downward-propagating signals appear above 1 hPa, reach approximately 3 hPa (~41 km) at lag = −4, and disappear thereafter in the stratosphere. At lag = −9, the ZWN-2 and $\omega = 1$ components of Z' (shading) are in quadrature with those of the downward-propagating PWs (contour) in the USLM. This confirms that the downward-propagating PWs are generated by Z' in the USLM in that the tendency of q' is in quadrature with Z' (i.e., $\partial q'/\partial t \propto -iq' \propto Z'$) and q' is proportional to $-H'$ (i.e., $q' \propto \nabla^2\psi' \propto -\psi' \propto -H'$) as in Eqs. (9) and (10).

Figure 14 shows temporal variations in the amplitudes of H's with ZWN-2 and $\omega = 0$ (Figs. 14a–c) or 1 (Figs. 14d–f) during the evolution of SSW09. The PWs of ZWN-2 with stationary components have features similar to those of all ZWN-2 PWs, as shown in Fig. 4b: (i) enhanced amplitudes above 30 km at around lag = −5 and (ii) long-lasting enhanced amplitudes below 30 km. The stationary components mainly propagate upward except in the upper stratosphere after the central date and near the tropopause from mid-December to mid-January. On the other hand, the $\omega = 1$ components have two peaks over z = 30–50 km at around lag = −12 and lag = −2 with relatively smaller magnitudes than the stationary components. As shown in Fig. 12, the $\omega = 1$ components have mixed structures of the upward- and downward-propagating PWs. The downward-propagating PW with the $\omega = 1$ components can be found in 4 regions: (i) near the tropopause, (ii) above 30 km in early–mid-December, (iii) above 50 km at approximately lag = −20, and (iv) above 35 km during lag = −10 to lag = −4. In particular, the regions of (ii)–(iv) are consistent with the regions where the enhanced ZWN-2 patterns of Z' appear in Fig. 10. The strongest downward-propagating PW signals in region (iv) gradually descend from 0.1 hPa at lag = −10 and reach 5–3 hPa at approximately lag = −5, where the maximum value

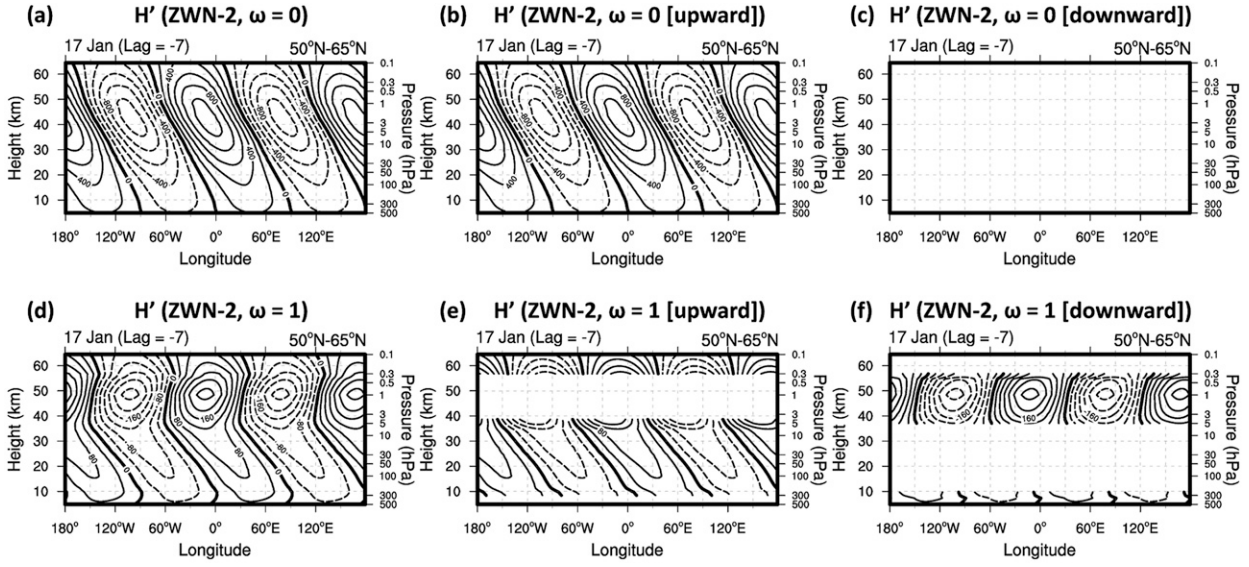

FIG. 12. Longitude–height cross sections of geopotential height perturbations (H') of zonal wavenumber 2 decomposed into (a)–(c) stationary ($\omega = 0$) and (d)–(f) $\omega = 1$ components (corresponding to a period of 11 days) averaged over 50°–65°N at 17 Jan 2009 (lag = −7). Each H' is separated into (b),(e) upward- and (c),(f) downward-propagating components based on the sign of the vertical component of the EP fluxes in the area. The contour intervals in (a)–(c) and (d)–(f) are 200 and 40 m, respectively. See the text for more details about the methodologies of the 2D wave decomposition and separation into the upward- and downward-propagating waves.

of the PWs of ZWN-2 and stationary components appear, as shown in Fig. 12b. This coincidence of the enhanced Z' and the downward-propagating PWs of ZWN-2, especially just before the central date in the stratosphere, suggests the potential for PW generation by the NCGWD forcing in the USLM and their effects on the amplification of the PWs in the stratosphere before the central date of SSW09.

To examine whether the downward-propagating PWs in the USLM are related to other mechanisms, such as wave reflection or in situ generation by the baroclinic instability process, the refractive index squared (n_k^2) and the meridional PV gradient ($\partial\overline{q}/a\partial\phi$) given by (11) are considered. The refractive index squared associated with specific k is given by the following equation:

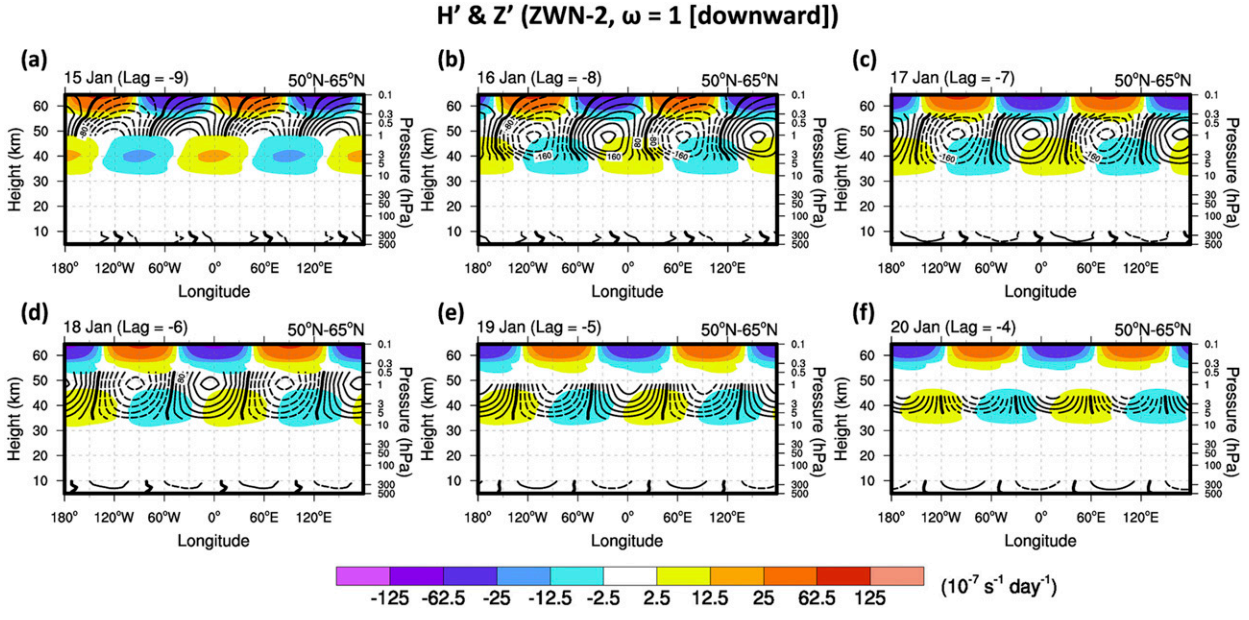

FIG. 13. Longitude–height cross sections of geopotential height perturbations (H'; contours) and nonconservative GWD forcing (Z'; shading) of zonal wavenumber 2 and $\omega = 1$ component averaged over 50°–65°N from 15 to 20 Jan 2009 (corresponding to lag = −9 to lag = −4). Only the downward-propagating H', which is separated based on the sign of the vertical component of the EP flux is represented.

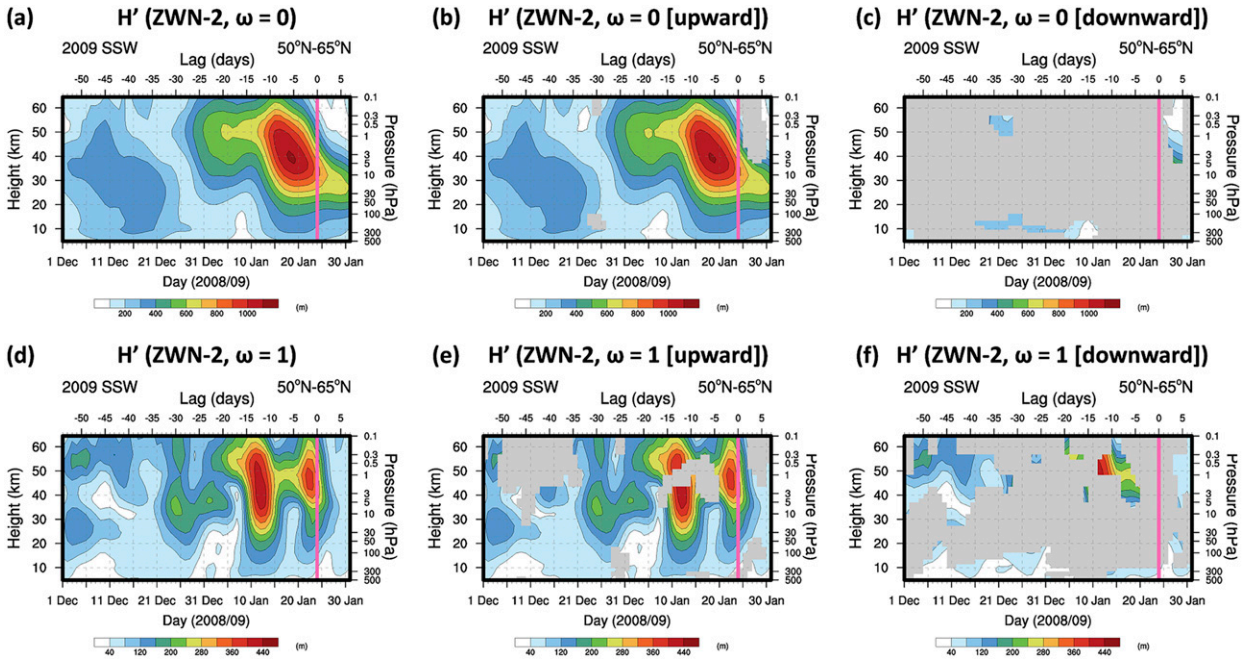

FIG. 14. Time–height cross sections of the amplitudes of the geopotential height perturbations (H's) for zonal wavenumber 2 with (a)–(c) $\omega = 0$ and (d)–(f) $\omega = 1$ averaged over 50°–65°N. The amplitudes of the H's for the specific wavenumber and frequency are separated into (b),(e) upward- and (c),(f) downward-propagating components. The contour intervals in (a)–(c) and (d)–(f) are 100 and 40 m, respectively. The pink solid lines denote the central date of the 2009 SSW event (lag = 0; 24 Jan 2009).

$$n_k^2(\phi, z) = \frac{1}{(\overline{u} - c)} \frac{\partial \overline{q}}{a \partial \phi} - k^2 - \left(\frac{f}{2NH} \right)^2. \tag{17}$$

Here, the phase speed (c) is determined by dividing ω by k. In general, PWs can propagate vertically or latitudinally in positive n_k^2 regions, while they are reflected in regions where n_k^2 changes its sign. Additionally, note that a negative $\partial \overline{q}/a\partial\phi$ is a necessary condition for baroclinic instability (Andrews et al. 1987).

Figure 15 shows latitude–height cross sections of the Z' decomposed into ZWN-2 components with stationary ($\omega = 0$) and $\omega = 1$ at lag = −7. The vectors in black indicate the EP fluxes corresponding to each ω component. The magenta and blue contours represent the zero n_k^2 ($k = 2$ in this figure) and zero $\partial \overline{q}/a\partial\phi$ lines, respectively. The EP flux vectors of the stationary ZWN-2 PWs are similar to those of the total ZWN-2 PWs revealed in Fig. 5c: upward and equatorward propagation into the stratosphere at latitudes lower than 70°N, avoiding strong PNJ in the high latitudes. The maximum of Z' with $\omega = 0$ exists near 65°N, while Z' with $\omega = 1$ has two peaks at 50°–60°N and 70°–85°N in the USLM. The peak of Z' at 70°–85°N may not be associated with the vertically propagating PWs given that a negative n_k^2s appears in these regions. On the other hand, poleward- and downward-propagating PWs mostly appear from the peak of Z' located in the USLM at 50°–60°N within the positive n_k^2 regions, implying the generation of the PWs by Z' in the USLM and their downward propagation into the midstratosphere. Although a small portion north of the peak Z' near 55°–60°N in the lower mesosphere is included in the regions of baroclinic instability (within thick blue contours), the baroclinic instability is unlikely related to the poleward- and downward-propagating PWs at 50°–65°N, considering the directions of EP flux vectors. The downward-propagating PWs are mainly shown at 50°–65°N and descend to approximately 5 hPa (~37 km). The downward-propagating PWs generated in the USLM and their poleward propagation into the stratosphere during lag = −9 to −5 can be clearly seen in Fig. 15c. Although the magnitude of the EP flux of the $\omega = 1$ component is one order smaller than that of the stationary component, the role of the downward-propagating PWs on the amplification of the ZWN-2 PWs in the stratosphere is not negligible, as the magnitude of PWs of $\omega = 1$ is not much smaller than that of the stationary component (see Figs. 12 and 13). The amplitude of the downward-propagating $\omega = 1$ component of ZWN-2 PWs is approximately 10%–20% of the upward-propagating stationary ZWN-2 PWs. Therefore, the downward-propagating PWs can act as an additional (but not negligible) contributor to enhanced PWs of ZWN-2 in the stratosphere during the evolution of SSW09. The downward-propagating eastward and poleward traveling PWs generated in situ from the NH winter mesosphere are also shown in Sato and Nomoto (2015, their Fig. 10a), although the generation of PWs is explained primarily by the baroclinic instabilities and PW generation and propagation are mostly between z = 60–70 km without propagating down to the stratosphere, contrary to the present study.

Figure 16a shows the simultaneous enhancement of Z' of ZWN-2 and $\omega = 1$ in the USLM and the downward-

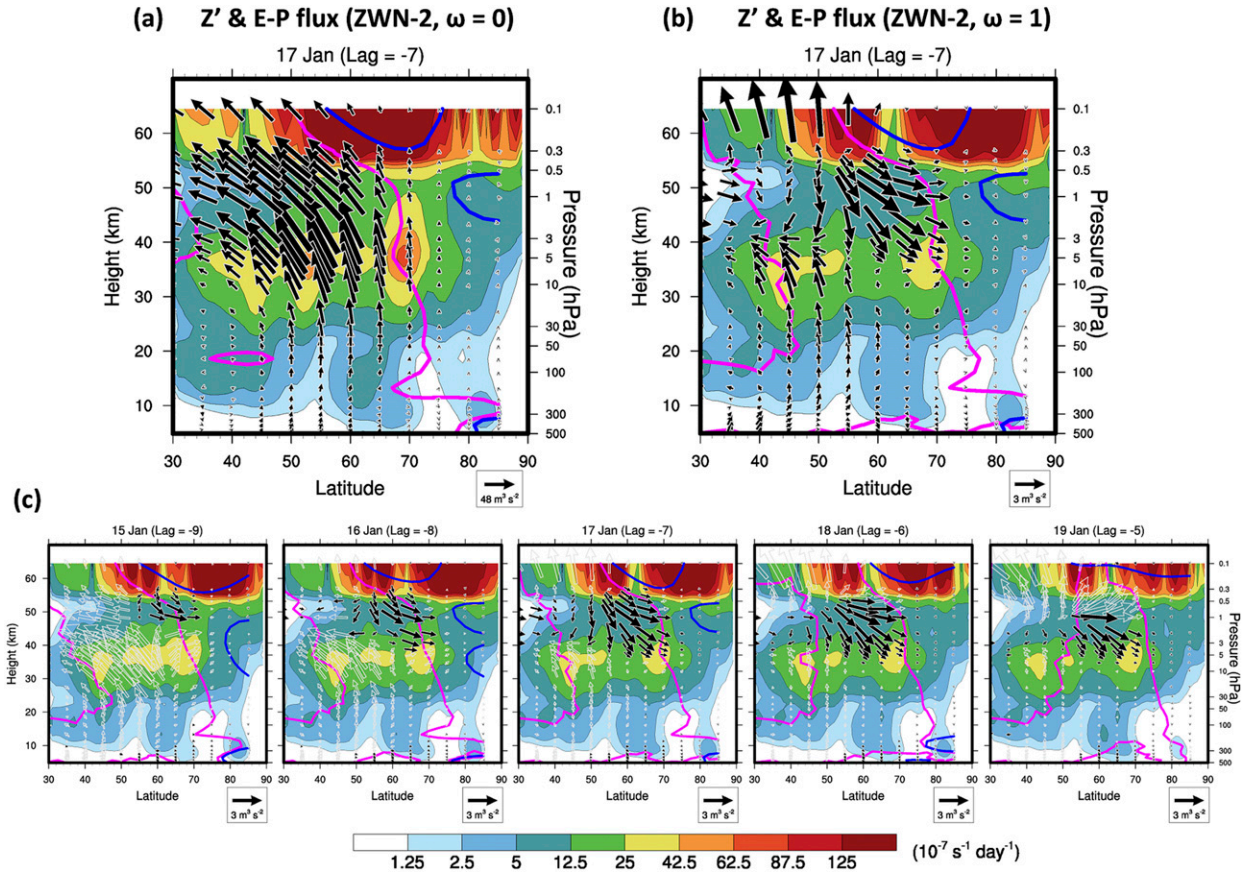

FIG. 15. Latitude–height cross sections of the nonconservative GWD forcing Z' and the EP fluxes (black vectors) by zonal wavenumber 2 with frequencies of (a) $\omega = 0$ and (b) $\omega = 1$ on 17 Jan 2009 (lag = −7). Note that the magnitude of the reference vector in (a) is 16 times larger than that in (b). The thick magenta and blue contours indicate zero refractive index (n_k^2) and zero meridional PV gradient [$\partial\overline{q}/(a\partial\phi)$], respectively. (c) As in (b) but during lag = −9 to lag = −5. Only the downward-propagating PWs denoted by black vectors in (c).

propagating PWs into the midstratosphere during the evolution of SSW09. Note that the directions of the positive x and z axes indicate the poleward and upward propagations of the EP flux (vector), respectively. To highlight the downward-propagating PWs, the EP fluxes with positive $F^{(z)}$ are not plotted. The Z' and EP fluxes are averaged over 50°–60°N and 50°–65°N, respectively, considering the potential source regions of the downward-propagating PWs in the USLM and the poleward-/downward-propagating PWs in the midstratosphere, as shown in Fig. 15b. Enhancements of the Z' in the USLM and downward-propagating PWs with ZWN-2 and ω = 1 are found in mid-December 2008 and mid-January 2009. The downward-propagating PWs, which are mainly directed toward the equator during December, begin to propagate poleward near lag = −9 and reach approximately 5 hPa at lag = −5. The temporal variation of Z' of ZWN-2 and $\omega = 1$ calculated using CERA-SAT forecasts is shown in Fig. S1d, which is qualitatively similar to Fig. S1c (same as Fig. 16a). However, the peak of Z' in CERA-SAT appears slightly earlier than that of MERRA-2 (Figs. S1a,b), and the peak of Z' in CERA-SAT is located slightly lower than that at 0.1 hPa in MERRA-2. The simultaneously enhanced Z' of ZWN-2 and $\omega = 1$ and the downward-propagating PWs in the USLM are seen in both MERRA-2 reanalysis and CERA-SAT forecasts. Figure 16b shows the Z' of ZWN-2 and $\omega = 1$ overlaid with the regions (gray) where the downward-propagating PWs appear. The H's larger than 35 m are shown in this figure. The yellow arrow represents a vector with a vertical group velocity of 5.5 km day^{-1}, which corresponds to the group velocity of vertically propagating Rossby waves of ZWN-2, as shown in Esler and Scott (2005).

Although the analyses of the traveling PWs are conducted for ZWN-2 components exclusively for the present study, in order to explain rapidly enhancing PWs of ZWN-2 in the stratosphere associated with SSW09, we additionally calculated traveling PWs in the USLM for PWs of ZWN-1 of which most previous studies on the PWs in the winter mesosphere are interested in (e.g., Sassi et al. 2012), and the results are shown in Fig. S2. As expected from the amplitude of PWs, as shown in Figs. 3 and 4, the amplitude of $F^{(z)}$ by the total ZWN-1 ($\sim 0.2 \times 10^4$ km s^{-2}) are significantly smaller than that by total ZWN-2 ($\sim 3.0 \times 10^4$ km s^{-2}). Interestingly, however, eastward- and upward-propagating traveling PWs with periods around 10 day are predominant to the stationary

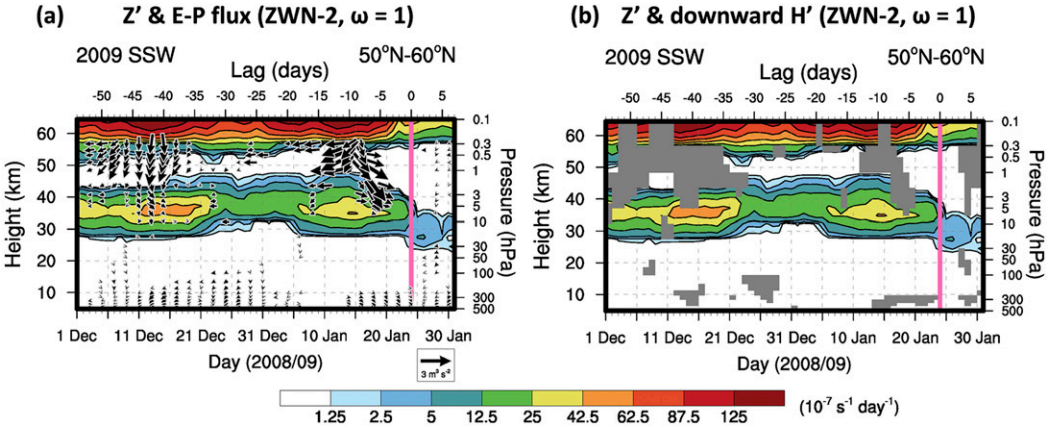

FIG. 16. (a) Time–height cross sections of the amplitude of Z' (shading) and EP fluxes (vectors) for zonal wavenumber 2 with a frequency component of $\omega = 1$. The Z' and EP fluxes are averaged over 50°–60°N and 50°–65°N, respectively. Only downward-propagating EP fluxes are shown. (b) As in (a), but for the gray regions where the downward-propagating H' exists. The yellow arrow indicates a group velocity of 5.5 km day^{-1}. The pink solid lines denote the central date of the 2009 SSW event (lag = 0; 24 Jan 2009).

PWs as well as downward-propagating traveling PWs for ZWN-1, contrary to the ZWN-2 case. Although the upward-propagating PWs of ZWN-1 in the USLM that are generated in situ from the nonconservative forcing of QGPV equation may not contribute to the rapid enhancement of PWs of ZWN-2 in the stratosphere during SSW09, they may contribute to the mesospheric circulation by providing positive EPD in the zonal wind for the recovery stage of SSW09. This is an interesting subject for the future research.

5. Summary and discussion

The SSW accompanied by a record-breaking temperature and wind change occurred on 24 January 2009. During the evolution of the SSW event, the polar vortex surrounding the Arctic regions has been broken up and clearly split into two parts. As the polar vortex breaking evolves, cold air confined within the vortex is split into two areas, while warm air intrudes into polar regions, which suddenly increases the polar air temperature by more than 50 K. The split-vortex structure and temperature increase are associated with the PW structures with ZWN-2.

At around lag = −5, the PWs of ZWN-2 are rapidly enhanced, while the PWs of ZWN-1 are significantly weakened in the stratosphere. These characteristics of the evolution of the ZWN-1 and ZWN-2 PWs can be found throughout a vertical range from 0.1 to 10 hPa, with maximum values at 3 hPa. The ZWN-2 PWs deposit strong westward forcing in the stratosphere during the evolution of the SSW09, even though the ZWN-1 PWs provide much stronger forcing than the ZWN-2 PWs during the normal winter.

The contributions of GWs to the evolution of the ZWN-1 and ZWN-2 PWs during the pre-SSW stage of SSW09 are investigated using the parameterized GWD provided by MERRA-2. During lag = −30 to −5, strong negative (westward) GWD_X exist in the high-latitude upper stratosphere with a magnitude larger than 20 m s^{-1} day^{-1}. Secondary maximum regions of negative GWD_X are located at 60°–70°N and 5–3 hPa (~35–40 km) with a magnitude of approximately 5 m s^{-1} day^{-1}. The mountains in high latitudes of the NH and strong westerly jets during the winter season seem to be associated with the strong negative GWD in the stratosphere. During the pre-SSW period, a high percentage of GWD_X to the total wave forcing up to approximately 90% is found in the high-latitude stratosphere.

The role of the GWD on the PWs in the stratosphere during the pre-SSW stage is investigated by analyzing the NCGWD forcing in the QGPV equation (Z'). Clear ZWN-2 patterns of Z' are found, especially in the USLM, prior to the onset of SSW09. To examine the characteristics of PWs generated by NCGWD forcing, a 2D Fourier wave decomposition is conducted on PWs using the 11-day time window moving daily for two months during December 2008–January 2009 to separate the upward- and downward-propagating components. During lag = −13 to lag = 0, enhanced upward propagations of the ZWN-2 PWs from the troposphere to the stratosphere are found, which are mainly from the stationary component. On the other hand, downward-propagating PWs of ZWN-2 with a period of 11 days appear in the USLM around lag = −10 and then gradually descend to the midstratosphere. Albers and Birner (2014) demonstrated that SSW09 can be caused by wave resonance, which is characterized by wave reflection and trapped wave energy in the stratosphere. Although this possibility is examined by calculating the refractive index squared (n_k^2) and the meridional PV gradient ($\partial\overline{q}/a\partial\phi$), the areas of negative n_k^2 and $\partial\overline{q}/a\partial\phi$ are sufficiently apart from the downward-propagating PWs. The downward PWs in the USLM are likely generated by the NCGWD forcing, given that the downward-propagating PWs are accompanied by the enhanced Z' in the USLM (see Fig. 16) and the phase structures of the downward-propagating H' are similar to the Z' (see Fig. 13).

Several previous studies have shown the possibility of generation of PWs in the stratosphere or the mesosphere by barotropic/baroclinic instabilities. Sato and Nomoto (2015)

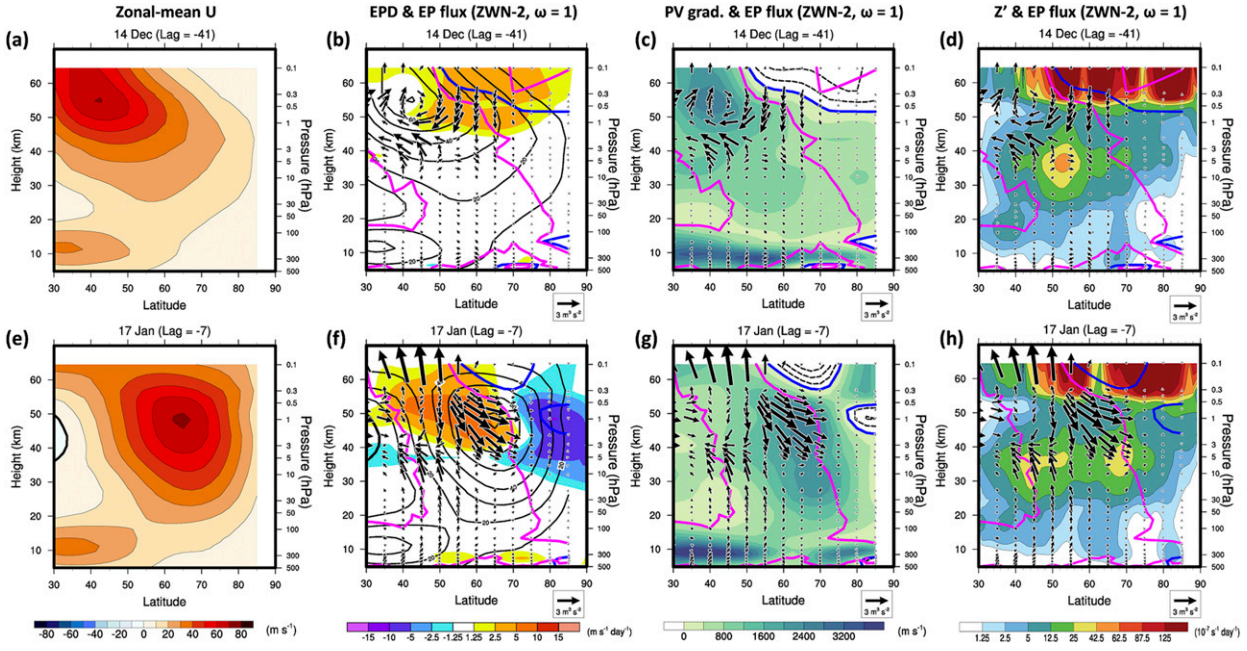

FIG. 17. Latitude–height cross sections of (a),(e) zonal-mean zonal wind, (b),(f) EPD, (c),(g) meridional PV gradient, and (d),(h) amplitude of Z' (shading) with EP fluxes (vectors) by ZWN-2 and $\omega = 1$ on (a)–(d) 14 Dec (lag = −41) and (e)–(h) 17 Jan (lag = −7). The thick magenta and blue contours indicate zero refractive index and zero meridional PV gradient, respectively.

demonstrated that anomalous westward GWD in the mesosphere induce cooling in the midlatitudes, leading to negative meridional PV gradient in the mesosphere. However, such GW-forced baroclinic instability is not observed during the evolution of SSW09. Garcia et al. (2005) showed generation of the PWs with 4-day period in the mesosphere and lower thermosphere (MLT) by instability using SABER observation data. Liu et al. (2004), Chandran et al. (2013), and Sassi and Liu (2014) also showed PWs generation due to the baroclinic instabilities using numerical simulation. Rodas and Pulido (2017) performed statistical analysis of PW generation by instability in the SH using MERRA. In the presence of traveling PWs induced by instability, the traveling PWs can interact with stationary PWs. Smith (1985) demonstrated that the SSW can be triggered through constructive and destructive interference between stationary and transient PWs. Although wave transience as a source of wave-mean interaction is not considered in this study, it is noteworthy that the stationary and transient PW contribute simultaneously to the SSW09. Therefore, further study on wave amplification by interaction between two different waves should be a continuing research topic for SSW09 case.

Figure 17 shows the zonal-mean zonal wind (Figs. 17a,e), EPD (Figs. 17b,f), $\partial\overline{q}/a\partial\phi$ (Figs. 17c,g), and amplitude of Z' (Figs. 17d,h) with EP fluxes of ZWN-2 and $\omega = 1$ on 14 December (lag = −41) and 17 January (lag = −7) when downward-propagating PWs exist as revealed in Fig. 15. The possible source of PWs in the USLM during mid-December is not clearly distinguishable because the generated PWs are propagated from the regions of enhanced Z' and negative PV gradient. On the contrary, near the time of rapid enhancement of PWs of ZWN-2 in the stratosphere (lag = −7), the source regions (e.g., enhanced Z' regions) of the downward-propagating PWs are relatively far from the region where baroclinic instability can occurs. The positive EPD (Fig. 17b) by eastward-propagating in situ PWs on the poleward side of PV maximum (Fig. 17c) at lag = −41 is generally consistent with that shown in Fig. 10a of Sato and Nomoto (2015).

The downward-propagating PWs have magnitudes of approximately 10%–20% of the upward-propagating stationary PWs, which contribute to the wave amplification near 5 hPa where the strongest enhancement of the ZWN-2 PWs occurred during the SSW09. The downward-propagating signals are dominant in the PWs propagating eastward with a period of 11 days. The downward-propagating signals are also found at 12.5- and 8.3-day waves when 25-day time window is applied. The PWs with periods about 11 days have been reported in several previous studies: Sjoberg and Birner (2012) found that SSWs are preferentially generated by a wave forcing with a period of approximately 10 days, although they focused on a forcing in the troposphere, and Lu et al. (2017) showed that ZWN-2 and ZWN-3, with a period of approximately 10 days, play an important role in the resonant growth of PWs in the stratosphere. Pancheva et al. (2007, 2008) observed PWs with a period of 11 days as one of the three significant PW components that appeared in the polar stratosphere during SSW occurred in the winter of 2003–04. Kishore et al. (2012) demonstrated, using MERRA, that PWs with periods of 7–11 days and 7–13 days are one of the dominant PW components at 52 and 62 km, respectively, during the evolution of SSW09.

Prediction of the spatiotemporal evolution and intensity of SSW is important for weather prediction in the troposphere,

given that significant temperature and wind anomalies in the stratosphere can propagate down toward the troposphere on weekly time scale (Baldwin and Dunkerton 2001). Therefore, better understanding of the effects of GWs on SSW will contribute to the improved forecast of SSW and weather system. Kim and Flatau (2010) showed that the better forecasts of stratospheric circulation and troposphere–stratosphere coupling are attributed to a new unified orographic GWD scheme implemented in the Navy Operational Global Atmospheric Prediction System (NOGAPS). With the new unified GWD scheme, enhanced PW activity can be found in the upper levels (stratosphere and mesosphere), resulting in successful simulation of SSW09, compared with the operational version of NOGAPS which failed to simulate SSW09.

In the present study, we investigated the role of GWD on SSW09, focusing on the generation of traveling PWs by the NCGWD forcing in the QGPV equation, using the MERRA-2 global dataset. The results of this study can be extended further using the idealized GCM, which is currently underway.

Acknowledgments. This work was supported by the National Research Foundation of Korea (NRF) grant funded by the Korea government (MSIT) (2017R1A2B2008025) and by the Korea Polar Research Institute (KOPRI; PE19020/PE20100). The MERRA-2 dataset was obtained from https://gmao.gsfc.nasa.gov/reanalysis/MERRA-2/data_access/. The CERA-SAT dataset was obtained from https://www.ecmwf.int/en/forecasts/datasets/reanalysis-datasets/cera-sat.

REFERENCES

Albers, J. R., and T. Birner, 2014: Vortex preconditioning due to planetary and gravity waves prior to sudden stratospheric warmings. *J. Atmos. Sci.*, **71**, 4028–4054, https://doi.org/10.1175/JAS-D-14-0026.1.

Andrews, D. G., J. R. Holton, and C. B. Leovy, 1987: *Middle Atmosphere Dynamics*. International Geophysics Series, Vol. 40, Academic Press, 489 pp.

Baldwin, M. P., and T. J. Dunkerton, 2001: Stratospheric harbingers of anomalous weather regimes. *Science*, **294**, 581–584, https://doi.org/10.1126/science.1063315.

Bancalá, S., K. Krüger, and M. Giorgetta, 2012: The preconditioning of major sudden stratospheric warmings. *J. Geophys. Res.*, **117**, D04101, https://doi.org/10.1029/2011JD016769.

Butler, A. H., J. P. Sjoberg, D. J. Seidel, and K. H. Rosenlof, 2017: A sudden stratospheric warming compendium. *Earth Syst. Sci. Data*, **9**, 63–76, https://doi.org/10.5194/essd-9-63-2017.

Chandran, A., R. R. Garcia, R. L. Collins, and L. C. Chang, 2013: Secondary planetary waves in the middle and upper atmosphere following the stratospheric sudden warming event of January 2012. *Geophys. Res. Lett.*, **40**, 1861–1867, https://doi.org/10.1002/grl.50373.

Charlton, A. J., and L. M. Polvani, 2007: A new look at stratospheric sudden warmings. Part I: Climatology and modeling benchmarks. *J. Climate*, **20**, 449–469, https://doi.org/10.1175/JCLI3996.1.

Chun, H.-Y., Y.-H. Kim, H.-J. Choi, and J.-Y. Kim, 2011: Influence of gravity waves in the tropical upwelling: WACCM simulations. *J. Atmos. Sci.*, **68**, 2599–2612, https://doi.org/10.1175/JAS-D-11-022.1.

Cohen, N. Y., E. P. Gerber, and O. Bühler, 2014: What drives the Brewer–Dobson circulation? *J. Atmos. Sci.*, **71**, 3837–3855, https://doi.org/10.1175/JAS-D-14-0021.1.

Coy, L., S. D. Eckermann, K. W. Hoppel, and F. Sassi, 2011: Mesospheric precursors to the major stratospheric sudden warming of 2009: Validation and dynamical attribution using a ground-to-edge-of-space data assimilation system. *J. Adv. Model. Earth Syst.*, **3**, M10002, https://doi.org/10.1029/2011MS000067.

Duck, T. J., J. A. Whiteway, and A. I. Carswell, 1998: Lidar observations of gravity wave activity and Arctic stratospheric vortex core warming. *Geophys. Res. Lett.*, **25**, 2813–2816, https://doi.org/10.1029/98GL02113.

——, ——, and ——, 2001: The gravity wave–Arctic stratospheric vortex interaction. *J. Atmos. Sci.*, **58**, 3581–3596, https://doi.org/10.1175/1520-0469(2001)058<3581:TGWASV>2.0.CO;2.

Esler, J. G., and R. K. Scott, 2005: Excitation of transient Rossby waves on the stratospheric polar vortex and the barotropic sudden warming. *J. Atmos. Sci.*, **62**, 3661–3682, https://doi.org/10.1175/JAS3557.1.

Garcia, R. R., and B. A. Boville, 1994: "Downward control" of the mean meridional circulation and temperature distribution of the polar winter stratosphere. *J. Atmos. Sci.*, **51**, 2238–2245, https://doi.org/10.1175/1520-0469(1994)051<2238:COTMMC>2.0.CO;2.

——, R. Lieberman, J. M. Russell III, and M. G. Mlynczak, 2005: Large-scale waves in the mesosphere and lower thermosphere observed by SABER. *J. Atmos. Sci.*, **62**, 4384–4399, https://doi.org/10.1175/JAS3612.1.

Gavrilov, N. M., A. V. Koval, A. I. Pogoreltsev, and E. N. Savenkova, 2018: Simulating planetary wave propagation to the upper atmosphere during stratospheric warming events at different mountain wave scenarios. *Adv. Space Res.*, **61**, 1819–1836, https://doi.org/10.1016/j.asr.2017.08.022.

Gelaro, R., and Coauthors, 2017: The Modern-Era Retrospective Analysis for Research and Applications, version 2 (MERRA-2). *J. Climate*, **30**, 5419–5454, https://doi.org/10.1175/JCLI-D-16-0758.1.

Harada, Y., and T. Hirooka, 2017: Extraordinary features of the planetary wave propagation during the boreal winter 2013/2014 and the zonal wave number two predominance. *J. Geophys. Res. Atmos.*, **122**, 11 374–11 387, https://doi.org/10.1002/2017JD027053.

——, A. Goto, H. Hasegawa, N. Fujikawa, H. Naoe, and T. Hirooka, 2010: A major stratospheric sudden warming event in January 2009. *J. Atmos. Sci.*, **67**, 2052–2069, https://doi.org/10.1175/2009JAS3320.1.

Haynes, P., M. McIntyre, T. Shepherd, C. Marks, and K. Shine, 1991: On the "downward control" of extratropical diabatic circulations by eddy-induced mean zonal forces. *J. Atmos. Sci.*, **48**, 651–678, https://doi.org/10.1175/1520-0469(1991)048<0651:OTCOED>2.0.CO;2.

Hirooka, T., and I. Hirota, 1985: Normal mode Rossby waves observed in the upper stratosphere. Part II: Second antisymmetric and symmetric modes of zonal wavenumbers 1 and 2. *J. Atmos. Sci.*, **42**, 536–548, https://doi.org/10.1175/1520-0469(1985)042<0536:NMRWOI>2.0.CO;2.

Holton, J. R., 1980: The dynamics of sudden stratospheric warmings. *Annu. Rev. Earth Planet. Sci.*, **8**, 169–190, https://doi.org/10.1146/annurev.ea.08.050180.001125.

——, 1983: The influence of gravity wave breaking on the general circulation of the middle atmosphere. *J. Atmos. Sci.*, **40**, 2497–2507, https://doi.org/10.1175/1520-0469(1983)040<2497:TIOGWB>2.0.CO;2.

——, 1984: The generation of mesospheric planetary waves by zonally asymmetric gravity wave breaking. *J. Atmos. Sci.*, **41**, 3427–3430, https://doi.org/10.1175/1520-0469(1984)041<3427:TGOMPW>2.0.CO;2.

Kao, S. K., 1968: Governing equations and spectra for atmospheric motion and transports in frequency, wave-number space. *J. Atmos. Sci.*, **25**, 32–38, https://doi.org/10.1175/1520-0469(1968)025<0032:GEASFA>2.0.CO;2.

Kim, Y.-J., and M. Flatau, 2010: Hindcasting the January 2009 Arctic sudden stratospheric warming and its influence on the Arctic Oscillation with unified parameterization of orographic drag in NOGAPS. Part I: Extended-range stand-alone forecast. *Wea. Forecasting*, **25**, 1628–1644, https://doi.org/10.1175/2010WAF2222421.1.

——, S. D. Eckermann, and H.-Y. Chun, 2003: An overview of the past, present and future of gravity-wave drag parametrization for numerical climate and weather prediction models. *Atmos.–Ocean*, **41**, 65–98, https://doi.org/10.3137/ao.410105.

Kishore, P., I. Velicogna, M. Venkat Ratnam, J. H. Jiang, and G. N. Madhavi, 2012: Planetary waves in the upper stratosphere and lower mesosphere during 2009 Arctic major stratospheric warming. *Ann. Geophys.*, **30**, 1529–1538, https://doi.org/10.5194/angeo-30-1529-2012.

Limpasuvan, V., M. J. Alexander, Y. J. Orsolini, D. L. Wu, M. Xue, J. H. Richter, and C. Yamashita, 2011: Mesoscale simulations of gravity waves during the 2008–2009 major stratospheric sudden warming. *J. Geophys. Res.*, **116**, D17104, https://doi.org/10.1029/2010JD015190.

Lindzen, R. S., 1981: Turbulence and stress owing to gravity wave and tidal breakdown. *J. Geophys. Res.*, **86**, 9707–9714, https://doi.org/10.1029/JC086iC10p09707.

Liu, H. L., E. R. Talaat, R. G. Roble, R. S. Lieberman, D. M. Riggin, and J. H. Yee, 2004: The 6.5-day wave and its seasonal variability in the middle and upper atmosphere. *J. Geophys. Res.*, **109**, D21112, https://doi.org/10.1029/2004JD004795.

Lu, H., L. J. Gray, I. P. White, and T. J. Bracegirdle, 2017: Stratospheric response to the 11-yr solar cycle: Breaking planetary waves, internal reflection, and resonance. *J. Climate*, **30**, 7169–7190, https://doi.org/10.1175/JCLI-D-17-0023.1.

Manney, G. L., and Coauthors, 2009: Aura Microwave Limb Sounder observations of dynamics and transport during the record-breaking 2009 Arctic stratospheric major warming. *Geophys. Res. Lett.*, **36**, L12815, https://doi.org/10.1029/2009GL038586.

Martineau, P., S.-W. Son, M. Taguchi, and A. H. Butler, 2018: A comparison of the momentum budget in reanalysis datasets during sudden stratospheric warming events. *Atmos. Chem. Phys.*, **18**, 7169–7187, https://doi.org/10.5194/acp-18-7169-2018.

Matsuno, T., 1970: Vertical propagation of stationary planetary waves in the winter Northern Hemisphere. *J. Atmos. Sci.*, **27**, 871–883, https://doi.org/10.1175/1520-0469(1970)027<0871:VPOSPW>2.0.CO;2.

——, 1971: A dynamical model of the stratospheric sudden warming. *J. Atmos. Sci.*, **28**, 1479–1494, https://doi.org/10.1175/1520-0469(1971)028<1479:ADMOTS>2.0.CO;2.

McDonald, A. J., R. E. Hibbins, and M. J. Jarvis, 2011: Properties of the quasi 16 day wave derived from EOS MLS observations. *J. Geophys. Res.*, **116**, D06112, https://doi.org/10.1029/2010JD014719.

McFarlane, N. A., 1987: The effect of orographically excited gravity wave drag on the general circulation of the lower stratosphere and troposphere. *J. Atmos. Sci.*, **44**, 1775–1800, https://doi.org/10.1175/1520-0469(1987)044<1775:TEOOEG>2.0.CO;2.

McLandress, C., and N. A. McFarlane, 1993: Interactions between orographic gravity wave drag and forced stationary planetary waves in the winter Northern Hemisphere middle atmosphere. *J. Atmos. Sci.*, **50**, 1966–1990, https://doi.org/10.1175/1520-0469(1993)050<1966:IBOGWD>2.0.CO;2.

——, M. J. Alexander, and D. L. Wu, 2000: Microwave Limb Sounder observations of gravity waves in the stratosphere: A climatology and interpretation. *J. Geophys. Res.*, **105**, 11 947–11 967, https://doi.org/10.1029/2000JD900097.

Molod, A., L. Takacs, M. Suarez, J. Bacmeister, I.-S. Song, and A. Eichmann, 2012: The GEOS-5 atmospheric general circulation model: Mean climate and development from MERRA to Fortuna. NASA Tech. Rep. NASA/TM-2012-104606, Vol. 28, 115 pp., https://gmao.gsfc.nasa.gov/pubs/docs/tm28.pdf.

Onogi, K., and Coauthors, 2007: The JRA-25 Reanalysis. *J. Meteor. Soc. Japan*, **85**, 369–432, https://doi.org/10.2151/jmsj.85.369.

Pancheva, D., P. Mukhtarov, and B. Andonov, 2007: Zonally symmetric oscillations in the Northern Hemisphere stratosphere during the winter of 2003–2004. *Geophys. Res. Lett.*, **34**, L04807, https://doi.org/10.1029/2006GL028666.

——, and Coauthors, 2008: Latitudinal wave coupling of the stratosphere and mesosphere during the major stratospheric warming in 2003/2004. *Ann. Geophys.*, **26**, 467–483, https://doi.org/10.5194/angeo-26-467-2008.

——, P. Mukhtarov, B. Andonov, N. J. Mitchell, and J. M. Forbes, 2009: Planetary waves observed by TIMED/SABER in coupling the stratosphere–mesosphere–lower thermosphere during the winter of 2003/2004: Part 2—Altitude and latitude planetary wave structure. *J. Atmos. Sol.-Terr. Phys.*, **71**, 75–87, https://doi.org/10.1016/j.jastp.2008.09.027.

Randel, W. J., R. R. Garcia, and F. Wu, 2002: Time-dependent upwelling in the tropical lower stratosphere estimated from the zonal-mean momentum budget. *J. Atmos. Sci.*, **59**, 2141–2152, https://doi.org/10.1175/1520-0469(2002)059<2141:TDUITT>2.0.CO;2.

Rodas, C., and M. Pulido, 2017: A climatology of Rossby wave generation in the middle atmosphere of the Southern Hemisphere from MERRA reanalysis. *J. Geophys. Res. Atmos.*, **122**, 8982–8997, https://doi.org/10.1002/2017JD026597.

Ryoo, J.-M., and H.-Y. Chun, 2005: Stratospheric major sudden warmings revealed in NCEP reanalysis data for 41 years (1958-1999). *J. Korean Meteor. Soc.*, **41**, 173–190.

Sassi, F., and H. L. Liu, 2014: Westward traveling planetary wave events in the lower thermosphere during solar minimum conditions simulated by SD-WACCM-X. *J. Atmos. Sol.-Terr. Phys.*, **119**, 11–26, https://doi.org/10.1016/j.jastp.2014.06.009.

——, R. Garcia, and K. Hoppel, 2012: Large-scale Rossby normal modes during some recent Northern Hemisphere winters. *J. Atmos. Sci.*, **69**, 820–839, https://doi.org/10.1175/JAS-D-11-0103.1.

Sato, K., and M. Nomoto, 2015: Gravity wave–induced anomalous potential vorticity gradient generating planetary waves in the winter mesosphere. *J. Atmos. Sci.*, **72**, 3609–3624, https://doi.org/10.1175/JAS-D-15-0046.1.

Scheffler, G., M. Pulido, and C. Rodas, 2018: The role of gravity wave drag optimization in the splitting of the Antarctic vortex in the 2002 sudden stratospheric warming. *Geophys. Res. Lett.*, **45**, 6719–6725, https://doi.org/10.1029/2018GL077993.

Schepers, D., E. de Boisséson, R. Eresmaa, C. Lupu, and P. de Rosnay, 2018: CERA-SAT: A coupled satellite-era reanalysis. *ECMWF Newsletter*, No. 155, ECMWF, Reading,

UnitedKingdom, 32–37, https://www.ecmwf.int/en/newsletter/155/meteorology/cera-sat-coupled-satellite-era-reanalysis.

Scinocca, J., 2003: An accurate spectral nonorographic gravity wave drag parameterization for general circulation models. *J. Atmos. Sci.*, **60**, 667–682, https://doi.org/10.1175/1520-0469(2003)060<0667:AASNGW>2.0.CO;2.

Siskind, D. E., S. D. Eckermann, J. P. McCormack, L. Coy, K. W. Hoppel, and N. L. Baker, 2010: Case studies of the mesospheric response to recent minor, major, and extended stratospheric warmings. *J. Geophys. Res.*, **115**, D00N03, https://doi.org/10.1029/2010JD014114.

Sjoberg, J. P., and T. Birner, 2012: Transient tropospheric forcing of sudden stratospheric warmings. *J. Atmos. Sci.*, **69**, 3420–3432, https://doi.org/10.1175/JAS-D-11-0195.1.

Smith, A. K., 1985: Wave transience and wave-mean flow interaction caused by the interference of stationary and traveling waves. *J. Atmos. Sci.*, **42**, 529–535, https://doi.org/10.1175/1520-0469(1985)042<0529:WTAWMF>2.0.CO;2.

——, 2003: The origin of stationary planetary waves in the upper mesosphere. *J. Atmos. Sci.*, **60**, 3033–3041, https://doi.org/10.1175/1520-0469(2003)060<3033:TOOSPW>2.0.CO;2.

Song, B.-G., and H.-Y. Chun, 2016: Residual mean circulation and temperature changes during the evolution of stratospheric sudden warming revealed in MERRA. *Atmos. Chem. Phys. Discuss.*, https://doi.org/10.5194/acp-2016-729.

Thurairajah, B., R. L. Collins, V. L. Harvey, R. S. Lieberman, M. Gerding, K. Mizutani, and J. M. Livingston, 2010: Gravity wave activity in the Arctic stratosphere and mesosphere during the 2007–2008 and 2008–2009 stratospheric sudden warming events. *J. Geophys. Res.*, **115**, D00N06, https://doi.org/10.1029/2010JD014125.

Venkat Ratnam, M., T. Tsuda, C. Jacobi, and Y. Aoyama, 2004: Enhancement of gravity wave activity observed during a major Southern Hemisphere stratospheric warming by CHAMP/GPS measurements. *Geophys. Res. Lett.*, **31**, L16101, https://doi.org/10.1029/2004GL019789.

Wang, L., and M. J. Alexander, 2009: Gravity wave activity during stratospheric sudden warmings in the 2007–2008 Northern Hemisphere winter. *J. Geophys. Res.*, **114**, D18108, https://doi.org/10.1029/2009JD011867.

Wang, X., and S. S. Shen, 1999: Estimation of spatial degrees of freedom of a climate field. *J. Climate*, **12**, 1280–1291, https://doi.org/10.1175/1520-0442(1999)012<1280:EOSDOF>2.0.CO;2.

Whiteway, J. A., T. J. Duck, D. P. Donovan, J. C. Bird, S. R. Pal, and A. I. Carswell, 1997: Measurements of gravity wave activity within and around the Arctic stratospheric vortex. *Geophys. Res. Lett.*, **24**, 1387–1390, https://doi.org/10.1029/97GL01322.

Yamashita, C., H. L. Liu, and X. Chu, 2010: Gravity wave variations during the 2009 stratospheric sudden warming as revealed by ECMWF-T799 and observations. *Geophys. Res. Lett.*, **37**, L22806, https://doi.org/10.1029/2010GL045437.

Zülicke, C., E. Becker, V. Matthias, D. H. W. Peters, H. Schmidt, H.-L. Liu, L. de la Torre, and D. M. Mitchell, 2018: Coupling of stratospheric warmings with mesospheric coolings in observations and simulations. *J. Climate*, **31**, 1107–1133, https://doi.org/10.1175/JCLI-D-17-0047.1.